

1 Simulating carbon and water fluxes using a coupled process-based
2 terrestrial biosphere model and joint assimilation of leaf area index
3 and surface soil moisture

4 **Sinan Li**^{1,2}, **Li Zhang**^{1,3,*}, **Jingfeng Xiao**⁴, **Rui Ma**⁵, **Xiangjun Tian**⁶, **Min Yan**^{1,3}

5 ¹ Key Laboratory of Digital Earth Science, Aerospace Information Research Institute, Chinese Academy of Sciences, No. 9
6 Dengzhuang South Road, Beijing 100094, China.

7 ² College of Resources and Environment, University of Chinese Academy of Sciences, No. 19A Yuquan Road, Beijing 100049, China

8 ³ Key Laboratory of Earth Observation of Hainan Province, Sanya 572029, China

9 ⁴ Earth Systems Research Center, Institute for the Study of Earth, Oceans, and Space, University of New Hampshire, Durham, New
10 Hampshire 03824, USA

11 ⁵ School of Remote Sensing and Information Engineering, Wuhan University, Wuhan 430079, China

12 ⁶ International Center for Climate and Environment Sciences (ICCES), Institute of Atmospheric Physics, Chinese Academy of Sciences,
13 Beijing 100029, China

14
15 * Correspondence: zhangli@aircas.ac.cn; Tel.: +86-10-8217-8193
16
17
18

19 **Abstract:**

20 Reliable modeling of carbon and water fluxes is essential for understanding the terrestrial carbon
21 and water cycles and informing policy strategies aimed at constraining carbon emissions and improving
22 water use efficiency. We designed an assimilation framework (LPJ-Vegetation and soil moisture Joint
23 Assimilation, or LPJ-VSJA) to improve gross primary production (GPP) and evapotranspiration (ET)
24 estimates globally. ~~The terrestrial biosphere model we used to be the~~ The integrated model, LPJ-PM as
25 the underlying model, coupled from the Lund-Potsdam-Jena Dynamic Global Vegetation Model (LPJ-
26 DGVM version 3.01) and a hydrology module (i.e., the updated Priestley–Taylor Jet Propulsion
27 Laboratory model, PT-JPL_{SM}). Satellite-based soil moisture products derived from the Soil Moisture and
28 Ocean Salinity (SMOS) and Soil Moisture Active and Passive (SMAP) and leaf area index (LAI) from
29 the global Land and Ground satellite (GLASS) product were assimilated into LPJ-PM to improve GPP
30 and ET simulations using a Proper Orthogonal Decomposition-based ensemble four-dimensional
31 variational assimilation method (POD_{En4DVar}). The joint assimilation framework LPJ-VSJA achieved
32 the best model performance (with an R^2 of 0.91 and 0.81 and an ubRMSD reduced by ~~50.4~~40.3% and
33 ~~38.4~~29.9% for GPP and ET, respectively, compared with those of LPJ-DGVM at the monthly scale). The
34 assimilated GPP and ET demonstrated a better performance in the arid and semi-arid regions (GPP:
35 $R^2=0.73$, ubRMSD=1.05 g C m⁻² d⁻¹; ET: $R^2=0.73$, ubRMSD= 0.61 mm d⁻¹) than in the humid and sub-
36 dry humid regions (GPP: $R^2=0.61$, ubRMSD=1.23 g C m⁻² d⁻¹; ET: $R^2=0.66$; ubRMSD=0.67 mm d⁻¹).
37 The ET simulated by LPJ-PM that assimilated SMAP or SMOS had a slight difference, and the SMAP
38 soil moisture data performed better than that SMOS data. Our global simulation modeled by LPJ-VSJA

39 was compared with several global GPP and ET products (e.g., GLASS GPP, GOSIF GPP, GLDAS ET,
40 GLEAM ET) using the triple collocation (TC) method. Our products, especially ET, exhibited advantages
41 in the overall error distribution (estimated error (μ): 3.4 mm month⁻¹; estimated standard deviation of μ :
42 1.91 mm month⁻¹). Our research showed that the assimilation of multiple datasets could reduce model
43 uncertainties, while the model performance differed across regions and plant functional types. Our
44 assimilation framework (LPJ-VSJA) can improve the model simulation performance of daily GPP and
45 ET globally, especially in water-limited regions.

46 **Keywords:** Data Assimilation; SMOS; SMAP; Gross primary production (GPP); evapotranspiration
47 (ET); GLASS [LAI](#)

48

49 1. Introduction

50 Gross primary production (GPP) and evapotranspiration (ET) are essential components of the carbon
51 and water cycles. Carbon and water fluxes are inherently coupled on multiple spatial and temporal scales
52 (Law et al. 2002; Sun et al. 2019; Waring and Running 2010). [Terrestrial biosphere models](#) ~~Land surface~~
53 ~~models (LSMs)~~ are the most sophisticated approach for providing a relatively detailed description of such
54 interdependent relationships regarding water and carbon fluxes and understanding the response of
55 terrestrial ecosystems to changes in atmospheric CO₂ and climate (Kaminski et al. 2017). [The dynamic](#)
56 [global vegetable models \(DGVMs\) are process-based dynamic terrestrial biosphere models, which can](#)
57 [simulate material exchange between vegetation and different conditions from the perspective of](#)

58 vegetation physiological processes, and is—are widely used to estimate carbon and water fluxes of
59 terrestrial vegetation. However, there are still large uncertainties in carbon and water flux estimates at
60 regional to global scales. Both diagnostic and prognostic models show substantial differences in the
61 magnitude and spatiotemporal patterns of GPP and ET. For example, the global annual GPP estimates
62 exhibited a large range (130–169 Pg C yr⁻¹) among 16 process-based terrestrial biosphere models (Anav
63 et al. 2015). The global ET ranged from 70,000 to 75,000 km³ yr⁻¹, and the uncertainty of regional or
64 global ET estimates was up to 50% of the annual mean ET value, especially in the semi-arid regions
65 (Miralles et al. 2016). These uncertainties mainly arise from the forcing datasets, simplification of
66 mechanisms or imperfect assumptions in processes, and uncertain parameters in the processed models
67 and assimilation methods (Xiao et al. 2019).

68 In the last two decades, remote sensing products have been assimilated into DGVMs to reduce the
69 uncertainty in modeled carbon and water fluxes (MacBean et al. 2016; Scholze et al. (2017); Exbrayat
70 et al. (2019)). Data assimilation (DA) is an effective approach to reduce uncertainties in terrestrial
71 biosphere models by integrating satellite products with models to constrain related parameters or state
72 variables. A DA system contains three-four main components: a set of observations, an observation
73 operator, an underlying model, and an assimilation method. The assimilation method considers the errors
74 from both models LSMs and observations, and reduces model uncertainties by minimizing a cost function.
75 The Ensemble Kalman Filter (EnKF) has been widely applied in land surface process models for
76 parameter optimization, —which significantly improve simulations by periodically updating state
77 variables (e.g., LAI and soil moisture) using remote sensing data without altering the model structure

78 (Ines et al. 2013; Li et al. 2017; Ma et al. 2013). Yet, the EnKF relies on the instantaneous observations
79 to update the state variable at the current time, and gives the predicted value at the next time based on the
80 forward integration of the updated state variable. The four-dimensional variational method (4DVar)
81 assimilation method can obtain the dynamic balance of the estimation in the time window when it is
82 applied to the long-series forecast model (Barth et al. 2014; Zhang et al. 2014). In particular, the Proper
83 Orthogonal Decomposition (POD)-based ensemble 4DVAR assimilation method (referred to as
84 PODEn4DVar) (Tian and Feng 2015) requires relatively less computation and can simultaneously
85 assimilate the observations at different time intervals. Meanwhile, it maintains the structural information
86 of the four-dimensional space. This method has a satisfactory performance in land DA for carbon and
87 water variables (Tian et al. 2009; Tian et al. 2010) and can better estimate GPP and ET than ~~ENKF~~EnKF
88 (Ma et al. 2017).

89 Multiple sources of remote sensing data streams have been used to constrain models for assimilation.
90 As a critical biophysical parameter of the land, leaf area index (LAI) is closely related to many land
91 processes, such as photosynthesis, respiration, precipitation interception, ET, and surface energy
92 exchange (Fang et al. 2019). LAI is highly sensitive to the simulation of carbon and water fluxes (Liu et
93 al. 2018), and accurate LAI estimates can improve the simulations of the carbon and water fluxes (Bonan
94 et al. 2014; ~~Liu et al. 2018~~; Mu et al. 2007). ~~Soil moisture (SM) controls the process of surface infiltration~~
95 ~~and runoff, determines the amount of water that can be extracted from plant roots, and distributes the~~
96 ~~input energy into sensible heat flux and latent heat flux (Trugman et al. 2018). More accurate SM data~~
97 ~~can improve the simulation of hydrologic parameters (SM, Streamflow, etc.) (e.g., Brocca et al. 2012;~~

98 ~~Draper et al. 2011; Lee et al. 2011; Li and Rodell 2013~~). Soil moisture is a major driving factor affecting
99 vegetation production in arid ecosystems, especially, in semi-arid areas (Liu et al. 2020). Introducing
100 surface soil moisture (SSM) into the model can significantly improve GPP and ET simulation, particularly
101 in water-limited areas (He et al. 2017; Li et al. 2020).

102 The advancement of earth observation, machine learning, inversion algorithms, and computer
103 technology has improved the accuracy of global LAI products and boosted model-data fusion studies
104 (Fang et al. 2019; Kganyago et al. 2020; Xiao et al. 2017). The Advanced Very High-Resolution
105 Radiometer (AVHRR) generates global LAI products with the longest historic record (since the early
106 1980s). The GLASS LAI product has been verified to have a better accuracy than that of MODIS and
107 CYCLOPES and is more temporally continuous and spatially complete (Xiao et al. 2013). Several recent
108 studies showed that the assimilation of GLASS LAI into ~~terrestrial biosphere models~~DGVMs enhanced
109 the performance of the models in simulating carbon cycling (e.g., GPP, Net Ecosystem Exchange (NEE))
110 and hydrological (e.g., ET, SM) processes (Ling et al. 2019; Ma et al. 2017; Yan et al. 2016).

111 Microwave remote sensors are considered effective tools for measuring SM globally (Petropoulos et
112 al. 2015). For example, surface SM products have been derived from the Soil Moisture and Ocean Salinity
113 (SMOS) and Soil Moisture Active and Passive (SMAP) satellites equipped with an L-band microwave
114 instrument. The products from these satellites have been evaluated against in-situ observations and other
115 SM products and overall have high accuracy (Burgin et al. 2017; Cui et al. 2018). Additionally, the SMAP
116 performs better than SMOS and other SM products (e.g., Advanced Scatterometer (ASCAT), Advanced
117 Microwave Scanning Radiometer 2 (AMSR2)) with an overall lower error and a higher correlation based

118 on the verification with in-situ SM data from 231 sites (Cui et al. 2018; Kim et al. 2018). The assimilation
119 of SMAP data can improve the simulation accuracy of carbon and water fluxes (He et al. 2017; Li et al.
120 2020) and hydrological variables (surface soil moisture, root-zone soil moisture, and streamflow)
121 (Blyverket et al. 2019; Koster et al. 2018; Reichle et al. 2017). In addition, the assimilation of SMAP data
122 performed slightly better than that of SMOS and ESA CCI data (Blyverket et al. 2019).

123 In the nonlinear model or nonlinear observation operator, only simultaneous assimilation makes
124 optimal use of observations (MacBean et al. 2016). Therefore, a joint assimilation of soil moisture and
125 LAI can make full use of the two variables. From site (Albergel et al. (2010); Rüdiger et al. (2010); Wu
126 et al., 2018) to regional assimilation (Ines et al. (2013)), many studies have proposed that joint assimilation
127 of vegetation parameters and soil moisture is a potential improvement in modeling the carbon-water cycle.
128 For instance, ~~Ines et al. (2013) found that the joint assimilation of soil moisture and LAI achieved better~~
129 ~~results than the assimilation of one of the two variables.~~ joint assimilation of soil moisture and leaf area
130 index can improve the accuracy of crop yield estimation (Xie et al., 2018; Pan et al., 2019), with small
131 region and high spatial resolution, which adopting observation data from stations or high-resolution
132 satellites (e.g. Sentinel-1 and 2). ~~On~~ At a large regional scale, Bonan et al. (2020) assimilated LAI and SM
133 together into the Interactions between Soil, Biosphere and Atmosphere (ISBA) land model and improved
134 the modeled GPP, ET, and runoff in the Mediterranean region. Rahman et al. (2022) jointly assimilates
135 GLASS LAI and SMAP soil moisture to improve water and carbon flux simulations within
136 the Noah-MP model over the CONUS domain. Albergel et al. (2020) jointly assimilates the ASCAT soil
137 moisture index (SMWI) and LAI GEOV1 into ISBA (Interaction between Soil Biosphere and Atmosphere)

138 surface model through the Global Offline Land Data assimilation system LDAS-Model to monitor
139 extreme events such as drought and Heatwave events. In conclusion, Kalman Filter and its variant
140 methods are mostly used in regional scale joint assimilation methods at regional scale, which requires
141 many various kinds of observation data were chosen and the their its accuracy directly affects the
142 assimilation performance. However, no studies have examined the performance of assimilation of LAI
143 and SM into terrestrial biosphere models for improving the simulation of carbon and water fluxes at the
144 global scale.

145 In this study, we assimilated the SM products from both SMAP and SMOS and a LAI product (GLASS)
146 derived from AVHRR and MODIS into the LPJ-PM to improve the GPP and ET using the PODEn4DVar
147 method. We designed a new assimilation framework, LPJ-VSJA, which consists of three assimilation
148 schemes: (1) assimilation of LAI only, (2) assimilation of SM only, and (3) joint assimilation of LAI and
149 SM. Then, four experiments were performed based on global flux sites to evaluate the assimilation
150 performance. This study stems from the researches discussed above and further explored the potential of
151 joint assimilating satellite LAI and soil moisture products globally. Specifically, it was the first time that
152 an updated LPJ-DGVM model was used to jointly assimilate GLASS LAI and SMAP soil moisture for
153 and simulating global water and carbon fluxes. The latest global soil moisture datasets (SMOS and
154 SMAP) were used, and the assimilation performance of these two observations was analyzed. Since
155 previous work showed the vital importance of surface soil moisture in the semi-arid and arid areas, one of
156 tThe specific objectives of our study are is to: (1) evaluate the assimilation performance of three
157 assimilation schemes for estimating GPP and ET and further to select the optimal assimilation scheme;

158 ~~(2) compare the assimilation effect of the optimal assimilation scheme~~ in the humid and arid areas and
159 improved the understanding of the effect of surface soil moisture on vegetation activity in wet and dry
160 zones. ~~;~~ ~~(3) compare the assimilation capability in ET assimilation based on two microwave soil~~
161 ~~moisture products (SMOS and SMAP) (scheme 2); and (4) apply our LPJ-VSJA framework to simulate~~
162 ~~global carbon and water fluxes.~~ In addition, compared with the assimilation methods in previous studies
163 (mostly using Kalman Filter variants), the POD-En4DVar method is used, which greatly improves the
164 computational efficiency.

165 2. LPJ-VSJA framework and assimilation strategy

166 2.1. Coupled- model (LPJ-PM) for assimilation

167 In this study, a coupled terrestrial biosphere model, LPJ-PM, was used to simulate daily GPP and
168 ET by assimilating satellite-derived LAI and SM. The LPJ-PM is coupled from LPJ-DGVM and PT-
169 JPL_{SM}. The original input data in PT-JPL_{SM} were all inherited from LPJ-DGVM, with the exception of
170 relative humidity (RH) and surface soil moisture (SMOS and SMAP), including the initial LAI calculated
171 by the LPJ-DGVM or assimilated LAI obtained through the LAI assimilation scheme, canopy height, and
172 the fraction of absorbed photosynthetic effective radiation (fAPAR). The detailed processes of the LPJ-
173 PM have been described in Li et al. (2020), and the flow chart for the coupling is shown in Figure 1.

174 **Table 1. Description of the models and outputs in this study**

acronyms	Full name	Description	Output
----------	-----------	-------------	--------

LPJ-DGVM (Sitch et al. 2003)	Lund-Potsdam-Jena Dynamic Global Vegetation Model	This model is used as a model operator to simulated initial ET	GPP_{LPJ} , ET_{LPJ}
PT-JPL _{SM} (Purdy et al. (2018))	Updated Priestley– Taylor Jet Propulsion Laboratory model	The model is used as a module of the LPJ-PM and establishes a connection between SMAP SM and ET	N/A
LPJ-PM (Li et al. (2020))	Lund-Potsdam-Jena and Updated Priestley–Taylor Jet Propulsion Laboratory coupled model	An integrated model coupled from the PT-JPL _{SM} and LPJ-DGVM	GPP_{SM} , ET_{PM}
LPJ-VSJA (this study)	Lund-Potsdam-Jena Vegetation-Soil moisture-Joint - Assimilation system	A process-based assimilation framework for assimilating LAI and SSM jointly into LPJ- DGVM PM	GPP_{LAI} , ET_{LAI} ; GPP_{SM} , ET_{SM} ; GPP_{CO} ; ET_{CO}

[2.1.1 LPJ-DGVM](#)

The LPJ-DGVM is a process-oriented dynamic model, which considers mutual interaction of carbon and water cycling and is designed to simulate vegetation distribution and carbon, soil and atmosphere

179 fluxes (Sitch et al. 2003). For each plant functional type (PFT), the GPP is calculated by implementing
180 coupled photosynthesis and water balance

181 The canopy GPP is updated daily:

$$182 \quad GPP = \frac{(J_E + J_C - \sqrt{(J_E + J_C)^2 - 4\theta J_E J_C})}{2\theta} \quad (2.1)$$

183 where J_C is the Rubisco limiting rate of photosynthesis, J_E is the light limiting rate of photosynthesis, and
184 the empirical parameter θ represents the common limiting effect between the two terms. J_E is related to
185 APAR (absorbed photosynthetic radiation, product of FPAR and PAR), while J_C is related to V_{cmax}
186 (canopy maximum carboxylation capacity, $\mu \text{ mol CO}_2/\text{m}^2/\text{s}$):

$$187 \quad J_E = C_1 \text{APAR} \quad (2.2)$$

$$188 \quad J_C = C_2 V_{C \max} \quad (2.3)$$

189 where C_1 and C_2 are determined by a variety of photosynthetic parameters and the intercellular partial
190 pressure of CO_2 , which is related to atmospheric CO_2 content and further altered by leaf stomatal
191 conductance (Sitch et al. 2003). APAR and FPAR are directly related to LAI.

192 In the water cycle module, ET is calculated as the minimum of a plant- and soil-limited supply
193 function (E_{supply}) and the atmospheric demand (E_{demand}) (Haxeltine and Prentice 1996; Sitch et al.
194 2003). The soil structure is simplified to a “two-layer bucket” model (the top soil layer at a 0-50 cm depth
195 and the bottom layer at a 50-100 cm depth).

196
$$E_s = E_p \times W_{r20} \times (1 - f_v) \quad (2.4)$$

197 In this module, it is assumed that the soil layer above 20 cm produces water through evaporation,
198 and W_{r20} is the relative water content of the soil above 20 cm, which is used as the only soil water limit
199 for calculating vegetation transpiration and soil evaporation. In the evapotranspiration estimation, the
200 over-simplification of soil structure and soil water limitation lead to a large error (Sitch et al. 2003), while
201 LPJ-DGVM cannot directly assimilate surface soil water due to the limitation of soil layer stratification.

202 ~~The soil structure is simplified to a “two layer bucket” model (the top soil layer at a 0–50 cm depth and~~
203 ~~the bottom layer at a 50–100 cm depth), and therefore, the satellite-derived surface SM cannot be~~
204 assimilated into LPJ-DGVM directly. The oversimplified soil structure and single soil moisture limitation
205 inevitably lead to sizeable uncertainty in ET simulation. Additionally, the monthly input caused a daily
206 variation of the modeled SM, which was also not transmitted to the calculation of GPP and ET. Thus, the
207 updated PT-JPL model (hereafter referred to as PT-JPL_{SM}) was coupled with LPJ-DGVM and the model
208 structure was modified so that surface SM can be directly assimilated into the coupled model at the daily
209 time step.

210 2.1.2 PT-JPL_{SM}

211 In PT-JPL_{SM}, three ET components are modelled: soil evaporation (E), vegetation transpiration (T),
212 and leaf evaporation (I). The PT-JPL_{SM} introduced a constraint (0–1, C_{RSM}) of surface SM for T and E,
213 which was used to avoid the implicit soil water control (represented by $f_{SM} = RH^{VPD}$) in the PT-JPL model.

The constraint is determined by the amount of soil water available that depends on soil properties, surface SM, atmospheric conditions, potential ET (PET), and canopy height.

Vegetation transpiration:

$$C_{RSM} = (1 - RH^{4(1-VWC)(1-RH)})C_{SM} + (RH^{4(1-VWC)(1-RH)})C_{TRSM} \quad (2.5)$$

$$C_{TRSM} = 1 - \left(\frac{W_{CR} - W_{obs}}{W_{CR} - W_{pwp_CH}} \right)^{\sqrt{CH}} \quad (2.6)$$

where w_{obs} is the SMAP SM, w_{pwp} is the water content at the wilting point, and w_{fc} is the water content at field capacity, which is determined by the properties of the soil. W_{CR} is a crucial parameter in characterizing the extent of SM restriction on ET; w_{pwp_CH} is the canopy height (CH) and is related to the potential of roots capturing water from deeper sources to limit the transpiration rate and characterize the SM availability (Purdy et al., 2018; Evensen 2003; Serraj et al., 1999). The specific formula is given in Purdy et al. (2018).

Soil evaporation:

$$C_{RSM} = \frac{W_{obs} - W_{pwp}}{W_{fc} - W_{pwp}} \quad (2.7)$$

The proportion of available water limits the soil evapotranspiration to the maximum available water. This scalar was formulated to represent the relatively accurate extractable water content for the vegetation,

229 determined by soil properties and the water available for evaporation, which is estimated via surface water
230 constraints.

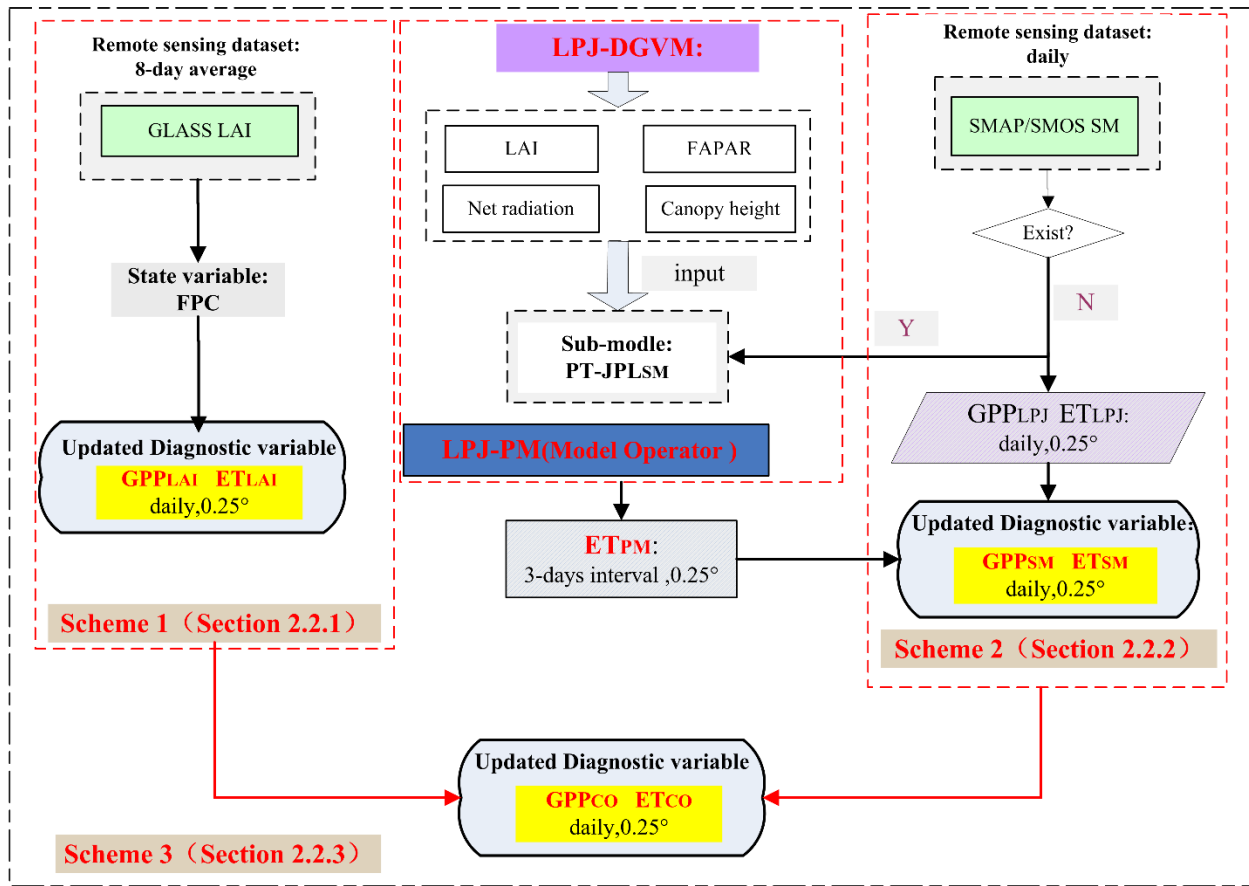
231 –The SMAP SM as surface SM data was applied to model global ET using PT-JPL_{SM} and the results
232 demonstrated the largest improvements for ET estimates in dry regions (Purdy et al. 2018). Due to the
233 limitation of soil stratification in LPJ-DGVM, the model was coupled with an updated remote-sensing
234 ET algorithm in the PT-JPL_{SM} that could better simulate ET in water-limited regions than in humid regions
235 (Purdy et al. 2018).

236 2.2. Assimilation scheme and experiment procedure

237 To improve the prediction capability of LPJ-PM, we designed three assimilation schemes:
238 assimilating LAI only (scheme 1, **output: ET_{LAI}, GPP_{LAI}**), assimilating ~~ET~~ SSM only (scheme 2, **output:**
239 **GPP_{SM}, ET_{SM}**), and joint assimilation of LAI and ~~ET~~ SSM (scheme 3, **output: ET_{CO}, GPP_{CO}**), i.e., LPJ-
240 VSJA framework) to test the assimilation performance for simulating GPP and ET.

241 The proposed LPJ-VSJA framework consists of four main components: the model operator (the LPJ-
242 PM), the observation operator (to establish the relation between the assimilation variable and the observed
243 variable), the observation series (GLASS LAI and SMOS or SMAP products), and the assimilation
244 algorithm (POD4DVar). With the surface soil moisture constraint in the PT-JPL_{SM}, the LPJ-VSJA
245 corrects the output fluxes (GPP and ET in this study).

LPJ-VSJA assimilation system



246

247

248

249

250

251

Figure 1. Flowchart of the LPJ-VSJA assimilation scheme: three assimilation schemes and the coupled model: LPJ-PM. (adapted from Li et al., 2020). The abbreviation of model and assimilation framework is explained in Table 1.

The experiment consisted of six steps:

252 ~~(1)~~Step 1: initialize the LPJ-DGVM and output the reference state variables without assimilation over
253 the experimental period (2010–2018), referred to as the “Control run” scenario;

254 Step 2: ~~(2)~~ implement schemes 1, 2, and 3, respectively, and the results represent the assimilation
255 integration state (daily GPP and ET assimilation results are referred to as the “GPP_{LAI}” and “ET_{LAI}” in
256 scheme 1; “GPP_{SM}” and “ET_{SM}” in scheme 2 and “GPP_{CO}” and “ET_{CO}” in scheme 3). This scenario used
257 the same input data and model parameter scheme with the “Control run” scenario;

258 Step 3: ~~(3)~~ evaluate GPP and ET results (schemes 1, 2 and 3) by comparing the parameters, R^2
259 (correlation coefficient), ~~RMSD (root mean square deviation)~~, BIAS, and ubRMSD (unbiased root mean
260 square deviation), for conditions of without-DA (“Control run” scenario) and with-DA states, and assess
261 the assimilation performance of separate assimilation (schemes 1 and 2) and joint assimilation (scheme
262 3) to determine the optimal assimilation scheme for GPP and ET, respectively;

263 Step 4: ~~(4)~~ evaluate the in-situ assimilated GPP and ET results where the sites are located in wet or
264 dry regions by dividing these validation sites into four parts (humid, sub-dry humid, semi-arid, and arid
265 regions), and this step was designed to assess the superiority of the proposed assimilation scheme in
266 water-limited areas;

267 Step 5: ~~(5)~~ compare the ET assimilation performance by assimilating the SMOS data with that by
268 assimilating the SMAP data.

269 Step 6: ~~and (6)~~ evaluate the simulated GPP and ET maps based on the optimal assimilation scheme
270 against existing global flux products.

271 2.2.1 DA scheme 1: LAI assimilation

272 In assimilation scheme 1, the observation operator determines the relationship between LAI and
273 foliage projective cover (FPC) in the process model (equation 2.1), and the assimilated LAI will be
274 propagated by energy transmission and ecosystem processes (e.g. photosynthesis, transpiration of
275 vegetative process) in the dynamic model to improve GPP and ET simulations (Bonan et al. 2014; Mu et
276 al. 2007). FPC, the vertically projected percentage of the land covered by foliage, regulates the rate of
277 photosynthate conversion and transpiration. In this study, the GLASS LAI with 8-day interval for the
278 period 2010–2018 was selected as the observation dataset for assimilation, and the FPC state variable was
279 updated daily through running the LPJ-PM (GPP_{LAI} , ET_{LAI} in this study) as shown below:

$$280 \quad FPC = 1 - e^{-0.5LAI} \quad (2.1)$$

281 We set the model and observation errors at a given time as 20% and 10% (scale factor) of the LAI
282 value and the observed LAI value, respectively. By verifying the assimilation performance (R, RMSD,
283 BIAS) for different scale factors (f) of model simulation and observations in the range of 0.05 to 0.40,
284 taking a step size of 0.05 (a total of 64 combinations), the optimal scale factors (0.2 and 0.1) were
285 determined (Bonan et al., 2020). The model and observation errors was the LAI value multiply by f. The
286 model integration generation method described by Pipunic et al. (2008) was used to determine the
287 minimum number of ensemble members required to achieve maximum efficiency, and the number of sets
288 was 20.

289 2.2.2 DA scheme 2: SSM assimilation

290 In this scheme, the surface SM products (SMOS or SMAP) were assimilated to LPJ-PM to obtain
291 more accurate ET (ET_{SM}) estimates in water-limited areas. The observation series was the SMOS or
292 SMAP SSM product, and the observation operator was the PT-JPL_{SM} model. The ET_{PM} estimated by the
293 coupled model (LPJ-PM) introducing surface SM was directly assimilated as a diagnostic variable. The
294 assimilated ET was applied to compute the top layer SM (50 cm) at the next time step (a nonlinear soil
295 water availability function described by Zhao et al. (2013), providing feedback for subsequent hydrologic
296 and carbon cycle processes. Then, the updated SM values regulated the GPP simulation (output: GPP_{SM}).
297 Different from other "constant" ET observations, the ET_{PM} ("observation") at each time t were adjusted
298 by absorbing intermediate variables updated after assimilation at time $t-1$. The ET_{PM} was shown to be
299 better than ET simulated by LPJ-DGVM but not as good as that simulated by the model with SMAP SM
300 assimilated (Li et al. 2020). Thus, it is proven that this SM assimilation schemes could improve the
301 accuracy of ET simulations.

302 All assimilation simulations were conducted between January 2010 and December 2018. Between
303 January 2010 and April 2015, SMOS data were used for assimilation; and after May 2015, both SMOS
304 and SMAP data were used for assimilation. An assimilation scheme was conducted when RH and SMOS
305 or SMAP SM data existed simultaneously; otherwise, the original simulation of the LPJ-DGVM was
306 conducted directly without adjustment of assimilation.

307 Similar to the LAI assimilation scheme, the model and observation errors were set as 15% and 5%
308 of ET_{LPJ} and ET_{PM} , respectively (LPJ-PM was adopted before assimilation). The number of ensembleset

309 members was set to 50. The ET_{PM} must be rescaled to the ET_{LPJ} distribution via their corresponding
310 cumulative probabilities using the cumulative distribution function (CDF) matching to avoid introducing
311 any bias in the LPJ-VSJA system (Li et al. 2020).

312 2.2.3 DA scheme 3: joint assimilation of LAI and SSM

313 In this scheme, both LAI from GLASS and SM from SMOS or SMAP were the observation datasets.
314 The GLASS LAI was assimilated by scheme 1 to obtain the FPC_{DA} and ET_{LAI} , and then the FPC_{DA} served
315 as input to LPJ-PM to simulate optimized ET_{PM} , and the ET_{LAI} was further assimilated with ET_{PM} to
316 generate ET_{CO} . Then, the SM (referred to as SM_{CO} in Figure S1) updated by ET_{CO} and the FPC_{DA} were
317 used as input to correct GPP (GPP_{CO}). ~~Finally, GPP_{CO} and ET_{CO} were output by joint assimilation based~~
318 ~~on the POD-En4DVar method.~~

319 Here, we applied the error regulation in scheme 1 and maintained the error setting of the LAI
320 observation and model simulation. Considering the transmission of integrated model error, we
321 recalculated the model error of LPJ-PM after the LAI assimilation and set model and observation errors
322 of ET_{LAI} and ET_{PM} to be 15 and 10%, respectively. ~~The number of set members was set to 70.~~

323 2.3. POD-Based Ensemble 4D Variational Assimilation Method

324 ~~The POD-En4DVar~~ The Proper Orthogonal Decomposition (POD)-based ensemble four-dimensional
325 variational (4DVar) assimilation method (referred to as POD-En4DVar) (Tian and Feng 2015) (Tian et al.
326 2011) method has the advantage of avoiding the calculation of adjoint patterns as its incremental analysis

field, which can be represented linearly by the POD base (Transformed OP (Observing Perturbation) and MP (Model Perturbation)), ~~and then saving computation~~. Moreover, the PODEn4DVar can simultaneously assimilate multiple-time observation data and provide flow-dependent (the flow-dependent is the ensembles of forecasting statistical characteristics in the t time) error estimates of the background errors. It has shown advantages in terrestrial assimilation, Tan-Tracker joint DA, and Radar assimilation (Tian et al. 2010; Tian et al. 2009; Tian et al. 2014; Zhang and Weng 2015).

By minimizing the following initial incremental format of the cost function in the 4DVar algorithm, an analysis field can be obtained:

$$J(x') = \frac{1}{2}(x')B^{-1}(x') + \frac{1}{2}[y'(x') - y'_{obs}]^T R^{-1}[y'(x') - y'_{obs}]$$

Here, the $x' = x - x_b$, $y'(x') = y(x' + x_b) - y(x_b)$, $y'_{obs} = y_{obs} - y(x_b)$, $y = H[M_{t_0 \rightarrow t_k}(x)]$. $x'(x'_1, x'_2, \dots, x'_N)$ is the model perturbation (MP) matrix and $y'(y'_1, y'_2, \dots, y'_N)$ is the observation perturbation (OP) matrix with N samples. Following Rüdiger et al. (2010), the LAI perturbation was set to a fraction (0.001) of the LAI itself. The perturbation of ET_{PM} and ET_{LPJ} conforms to a Gaussian distribution with a mean of 0 and a specified covariance (10 and 5% of the ET_{PM} and ET_{LPJ} at time t). The subscript b represents the background field, the superscript T represents a transpose, H is the observation operator of scheme 1 as described in section [2.3.2.2.1](#), and scheme 2 is the PT-JPL_{SM} (described in [Purdy et al. \(2018\) 2.1.2](#)). M is the forecast model (LPJ-PM in this study), B is the background error covariance, R is the observation error covariance, and obs denotes observation.

345 Assuming the approximately linear relationship between OP(y') and MP(x'), POD decomposition
 346 and transformation were successively conducted for OP and MP. The transformed OP samples ($\Phi_y =$
 347 y'_1, y'_2, \dots, y'_n) are orthogonal and independent, and the transformed MP samples ($\Phi_x =$
 348 x'_1, x'_2, \dots, x'_n) are orthogonal to the corresponding OP samples, where n is the number of POD modes.

349 The manifestation of the background error covariance is the same as the Ensemble Kalman filter
 350 (EnKF, Evensen (2004)), and the incremental analysis x'_a was expressed by the $\Phi_{x,n}$, and $\tilde{\Phi}_y$ ($\tilde{\Phi}_y =$
 351 $[(n-1)I_{n \times n} + \Phi_{y,n}^T R^{-1} \Phi_{y,n}]^{-1} \Phi_{y,n}^T R^{-1}$). Finally, the final-optimal analysis x_a is calculated as $x_a =$
 352 $x_b + \Phi_{x,n} \tilde{\Phi}_y y'_{obs}$. The detailed derivation process of the algorithm is described by a previous study (Tian
 353 et al. 2011).

354 In the ensemble-based method (Evensen et al., 2004), the number of ensemble members is usually
 355 fewer than that of the observation data and the degrees of freedom of the model variables, and spurious
 356 long-range correlations occur between observation locations and model variables. A practical method, the
 357 localization technique, is applied to address this issue (Mitchell et al. 2002). The final incremental analysis
 358 is rewritten as:

$$359 \quad x'_a = \Phi_{x,n} \tilde{\Phi}_y y'_{obs} C_0 \left(\frac{d_h}{d_{h,0}} \right) \cdot C_0 \left(\frac{d_v}{d_{v,0}} \right)$$

360 where d_h and d_v are the horizontal and vertical distances between the spatial positions of state and
 361 observed variables, respectively; and $d_{h,0}$ and $d_{v,0}$ are the horizontal and vertical covariance localization
 362 Schur radii, respectively. The filtering function C_0 is expressed as:

$$C_0(r) = \begin{cases} -\frac{1}{4}r^5 + \frac{1}{2}r^4 + \frac{5}{8}r^3 - \frac{5}{3}r^2 + 1, & 0 \leq r \leq 1, \\ \frac{1}{12}r^5 - \frac{1}{2}r^4 + \frac{5}{8}r^3 + \frac{5}{3}r^2 - 5r + 4 - \frac{2}{3}r^{-1}, & 1 \leq r \leq 2, \\ 0, & 2 < r \end{cases}$$

where r is the radius of the filter.

The assimilation algorithm is mainly divided into two steps: (1) prediction: run LPJ-PM in the current assimilation window and generate simulation results and background field vectors; (2) update: the algorithm is used to calculate the optimal assimilation increment x'_a and analysis solution x_a , and the simulation results and the initial conditions of the model in the current window are updated using the analysis solution. The updated initial conditions were applied for model LPJ-PM prediction, and the above process was repeated.

2.4. Validation method for assimilation performance

The R^2 (correlation coefficient), ~~RMSD (root mean square deviation)~~, Bias, and ubRMSD (unbiased root mean square deviation) between simulation and tower-based observations were applied for evaluation. In addition, a Taylor chart was also used to demonstrate the performance of two ET estimations with different SM observations in terms of R , ubRMSD, and Normalized Standard Deviation (NSD) on 2D plots, to display how closely the datasets matched observations in one diagram (Taylor 2001). In the Taylor diagram, SD represents the radial distance from the origin point and the correlation with the site observations as an angle in the polar plot. The ubRMSD is the distance between the observation and the model and is represented in the figure as a green semi-circular arc with point A as the

380 center of the circle. The closer the model point to the reference point (Point A), the better the performance.
381 This diagram is convenient and visual in evaluating multiple aspects of various models.

382 The error variance of GPP and ET products was estimated using the triple collocation (TC) approach
383 (Stoffelen 1998) to validate the global simulation in this study. The method has been extensively applied
384 in the study of hydrology and oceanography (Caires and Sterl 2003; Khan et al. 2018; O'Carroll et al.
385 2008; Stoffelen 1998), particularly in SM studies (Chan et al. 2016; Kim et al. 2018). The TC provides a
386 reliable platform for comparison of spatial assimilation results and in-situ measurements. In this
387 experiment, no calculation was performed on the non-vegetated areas where the correlation was lower
388 than 0.2 to have independent datasets and avoid correlated errors (crucial assumptions in TC) (Yilmaz
389 and Crow 2014).

390 In this study, the five products were divided into three product categories, including satellite product
391 (MODIS, GOSIF GPP), reanalysis product (GLASS, GLDAS) and data assimilation product (GLEAM
392 ET, LPJ-VSJA) (Li et al.,2018). One product in each category was selected to form a group to calculate
393 their error. The LPJ-VSJA product was set as the reference data.

394 For GPP products, GOSIF, GLASS, and LPJ-VSJA were treated as a group, and MODIS, GLASS
395 and LPJ-VSJA were treated as another group to calculate the errors; the final errors were determined by
396 the average of these two.

397 Similarly, to calculate the errors for ET, GLEAM, GLASS, and MODIS were chosen as a group;
398 LPJ-VSJA, GLDAS, and MODIS were treated as a group; LPJ-VSJA, GLASS and MODIS were

399 considered as a group. In order to reduce the influence of orthogonality hypothesis of error, the first and
400 third groups are for indirect and effective comparison between LPJ-VSJA product and GLEAM product.

401 **3. Experiment sites and data**

402 *3.1. Description of flux tower sites*

403 We screened over 300 EC flux sites across the globe from the FLUXNET2015
404 (<https://fluxnet.fluxdata.org/data/fluxnet2015-dataset/>), AmeriFlux (<http://public.ornl.gov/ameriflux>),
405 and the HeiHe river basin ([Liu et al. \(2018\)](#), <http://www.heihedata.org>) (~~Li et al. 2013~~) for the evaluation of
406 assimilation performance over the period from January 2010 to December 2018. The in-situ half-hourly
407 LE and GPP data from the sites were aggregated into daily data. The daily gap-filled data were excluded
408 if the percentage of gap-filled half-hourly values was more than 20%. Then we corrected the data of
409 energy non-closure by using the Bowen ratio closure method (Twine et al. 2000) to improve the energy
410 closure rate (Huang et al. 2015; Yang et al. 2020). The data were selected to cover the 2010–2018 period
411 with at least one year of reliable data, and the result from the error of assimilation is relative to the LE
412 value and seasonal variation (Purdy et al. 2018; Zou et al. 2017). It is essential to have available data
413 every month during a one-year period, and only days with less than 25% missing data were processed per
414 month (Feng et al. 2015). In addition, for flux tower data, the data were also excluded for the analysis if
415 the SMAP/SMOS SM data were not of good quality.

416 Finally, we identified a total of 105 sites across the globe encompassing five major biomes: grassland
417 (18 for GPP and 19 for ET), savanna (11), shrubland (4), forest (49 and 53), and cropland (13 and 14). In

418 the comparative analysis of the performance for simulating ET by assimilating SMOS and SMAP SM
419 data separately, we selected 46 AmeriFlux sites (Figure S3) with at least one year of reliable data from
420 2015 to 2018 based on the simultaneous availability of SMAP and SMOS data, including grassland (19),
421 savanna (11), shrubland (5), forest (23), and cropland (7). Figure S2 and S3 illustrate the location and
422 distribution of the 105 and 46 EC flux tower sites, respectively. A more detailed description is
423 summarized in the Supporting Information Table S1.

424 3.2. Remote sensing datasets: LAI and SM

425 The GLASS LAI product with an 8-day time step and 5 km resolution was derived from MODIS
426 and CYCLOPES surface reflectance and ground observations using general regression neural networks
427 (GRNNs) (Liang et al. 2013; Xiao et al. 2016). The verification of the product using the mean values
428 of high-resolution LAI maps showed that the GLASS LAI values were closer to these high-resolution
429 LAI maps (RMSD= 0.78 and $R^2= 0.81$). Therefore, the GLASS LAI product has satisfactory performance
430 and can be assimilated into terrestrial biosphere models.

431 The SMAP mission (Entekhabi et al. 2010) and SMOS mission (Jacquette et al. 2010), the two
432 dedicated soil moisture satellites currently in orbit equipped with L-band microwave instruments, provide
433 surface SM retrievals. We chose the SMOS-L2 product and the SMAP-L3-Enhanced product, which both
434 provide global coverage every three days for soil depth of 5 cm. Only good-quality SMAP and SMOS
435 data were used. The grid cells with water areas larger than 10% and those with less than 50% good-quality
436 data in one year were masked out, which alleviates the undesirable model simulations caused by the

437 decrease in SMAP retrieval accuracy (Chan et al. 2016; O'Neill et al. 2010). We only adopted the data
438 with an uncertainty below $0.1 \text{ m}^3 \text{ m}^{-3}$, in the actual range ($0.00\text{--}0.6 \text{ m}^3 \text{ m}^{-3}$), and the temperature of the
439 LSM observation layer (the second layer) was higher than $2 \text{ }^\circ\text{C}$ (Blyverket et al. 2019).

440 Both the GLASS LAI, SMOS and SMAP observations was resampled to 9 km for site simulation
441 and 0.25° for spatial simulation.

442 3.3. Model-forcing and validation datasets

443 In this study, the meteorological, soil property, and CO_2 concentration datasets were used to drive
444 the LPJ-PM. For site simulation, in order to maintain consistency with the SMAP Enhanced 3 Level
445 product (Entekhabi et al. 2010), model-forcing data were resampled to a 9 km spatial resolution based on
446 EASE-2 projection grid. In the global spatial simulation, the model-forcing datasets were interpolated to
447 0.25° based on the bilinear method to ensure the consistency of spatial representation. Table 2 provides
448 the spatial and temporal characteristics of the model-forcing datasets in the LPJ-PM (submodule: LPJ-
449 DGVM and PT-JPL_{SM}).

450

451 **Table 2. List of the selected forcing and remote-sensing datasets used in this study**

Datasets	Variable	Period	Spatial resolution	References
CRU TS v4.1 ^a	Cloud cover,	1901-	$0.5^\circ \times 0.5^\circ$	New et al.

	temperature, precipitation, wet day	1930		(2000), https://crudata.uea.ac.uk/cru/data/hrg/ (Etheridge et al. (1996); Keeling et al. (1995)) https://scrippsc.o2.ucsd.edu/data/atmospheric_co2/
Ice-core measurements and atmospheric observations at the Mauna Loa Observatory ^a	Atmospheric CO ₂ concentrations	1901- 2018	NA	Rienecker et al. (2011) (https://www.esrl.noaa.gov/pds/) Wieder et al. (2014) http://daac.ornl.gov
MERRA-2 ^a	Precipitation, surface temperature, cloud fraction, relative humidity	2010- 2018	0.5° × 0.625°	
HWSD (v121) ^b	Soil texture data	NA	1 km × 1 km	

SPL3SMP_E ^b	Surface soil moisture	2015.4– present	9 km×9 km	Entekhabi et al. (2010), (https://smap.jpl.nasa.gov/)
GLASS LAI ^{a,b}	Leaf area index	2010- 2018	5 km×5 km	Xiao et al. (2016), http://www.glass.umd.edu/Download.html)
SMOS_L3 CATDS ^b	Surface soil moisture	2010- present	25km×25 km	Jacquette et al. (2010), (https://earth.esa.int/eogateway/missions/smos)

452 ^a: forcing dataset for LPJ-DGVM

453 ^b: external input dataset for PT-JPL_{SM}

454

455 We used four global ET products and three global GPP products (Li et al. 2018; Li and Xiao 2019;
 456 Wang et al. 2017) that was resample to 0.25° to evaluate the performance of the model with the joint
 457 assimilation scheme. Table 3 shows the details of these GPP and ET products.

458 **Table 3. Global GPP and ET products for comparison in this study**

Product	Dataset	Temporal resolution	Spatial resolution	Retrieval algorithm	References
MOD17A2	GPP and ET	8-day average	1 km × 1 km	GPP: Based on the light use efficiency (LUE) model ET: Improved Penman formula	Running et al. (2004)
GLASS	GPP and ET	8-day average	5 km × 5 km	GPP: EC-LUE model ET: Combining five Bayesian averages based on process models (BMA)	Yuan et al. (2010)
GOSIF GPP	GPP	8-day average	0.05° × 0.05°	Estimated from solar-induced chlorophyll	Li and Xiao (2019)

				fluorescence with GPP-	
				SIF relationships	
GLDAS ET	ET	daily	0.25°× 0.25°	Processed model assimilation	Fang et al. (2009)
GLEAM v3a ET	ET	daily	0.25°× 0.25°	Processed model assimilation	Martens et al. (2017)

459

460 4. Results

461 4.1. Performance of LPJ-PM for simulating GPP and ET with the assimilation of LAI and soil moisture

462 4.1.1 Accuracy assessment of GPP for separate and joint assimilation

463 In general, the R^2 between GPP_{LPJ} and GPP_{OBS} was above 0.4 at most of the sites (62 sites) and
464 were relatively weak for some sites ($R^2 < 0.4$). The LAI assimilation improved the simulations at most
465 sites (R^2 value increased at 82 sites), particularly for sites in the U.S. and Europe (Figure 2). The R^2
466 improvement from the LAI assimilation (scheme 1) was superior to that from the SM assimilation
467 (Figure 2- R^2 (b) and (c)). The performance of the joint assimilation (scheme 3) was similar to that of
468 scheme 1. ~~The GPP assimilation performance in terms of RMSD between scheme 1 and scheme 2 was
469 not significantly different. For sites with no improvement in the separate assimilation (schemes 1 and
470 2), the RMSD, however, was improved in the joint assimilation (scheme 3) (Figure 2).~~ Sites (Figure 2-

471 BIAS (a)) showed positive bias ($GPP_{OBS} - GPP_{LPI}$) were mainly distributed in the humid and dry-sub
472 humid forest, grassland, and arid cropland regions, showing an underestimation for GPP_{OBS} . The
473 assimilation improved the accuracy for overestimated sites, but there was no significant improvement
474 for underestimated sites. The ubRMSD implied that the SM assimilation alone had a better performance
475 than the LAI assimilation alone, especially for sites in arid areas. The analysis of the above ~~four~~ three
476 statistical measures (R^2 , ~~RMSD~~, BIAS, and ubRMSD) indicated that the accuracy of joint assimilation
477 was much better than that of separate assimilation.

478 At the seasonal scale, all three assimilation schemes corrected the model trajectory and
479 significantly improved the growing season simulations, especially for peak values (IT-Tor, US-NR1,
480 US-NE1) (Figure 3). In addition, the linear fitting of GPP_{CO} and GPP_{OBS} on a monthly scale was closer
481 to 1:1 ($y = 0.92 + 21.66 p < 0.001$) than that of GPP_{LAI} ($y = 0.89 + 28.3, p < 0.001$) and GPP_{SM} ($y = 0.86$
482 $+ 41.70, p < 0.001$) (Figure S5). The results in Table S2 support the above analysis, and the joint
483 assimilation showed advantages in overall accuracy in both arid and humid areas.

484

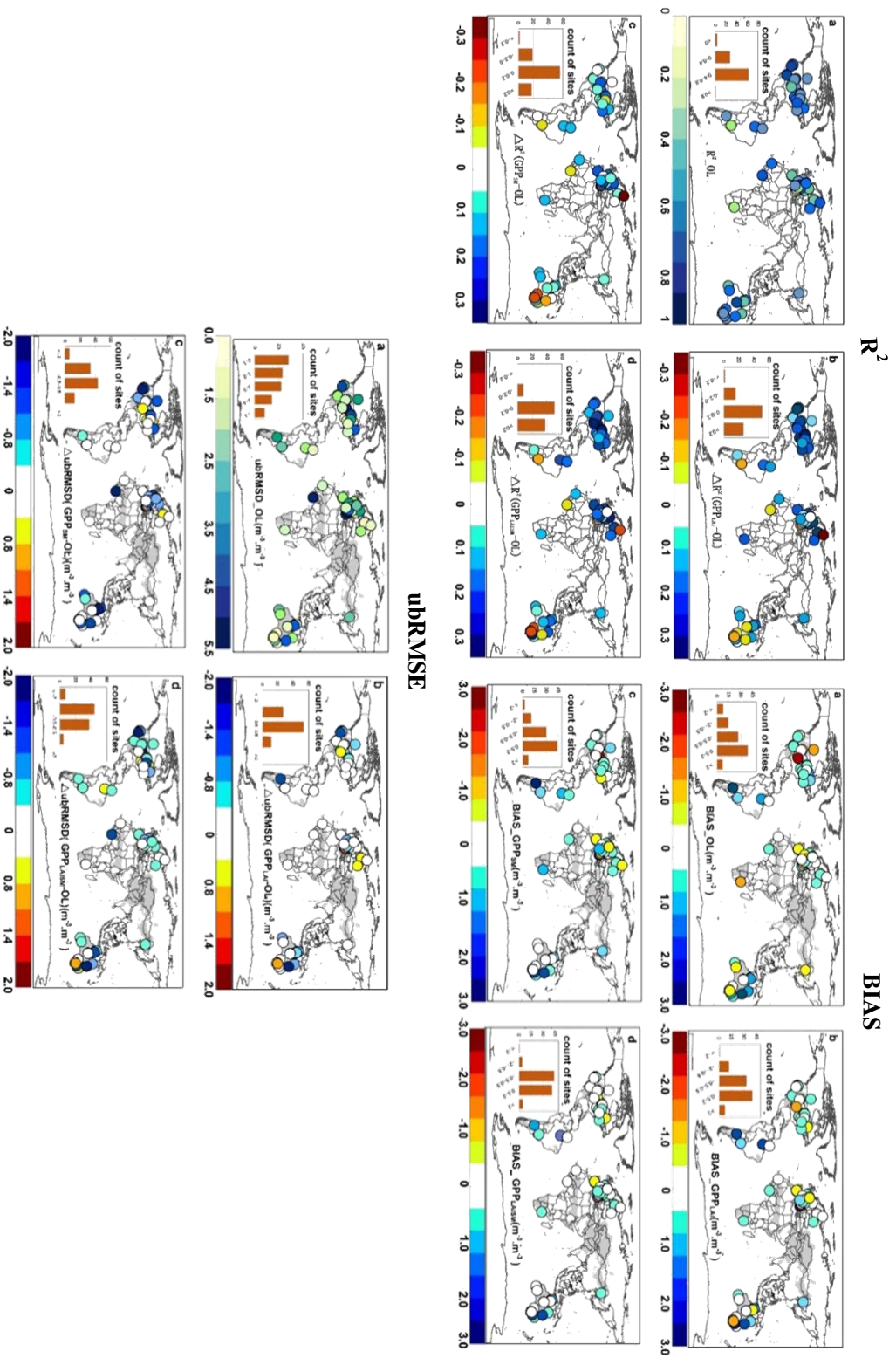


Figure 2 (a) The correlation coefficient (R^2), Bias and the Unbiased Root Mean Square Error (ubRMSE) between the $GPP(GPP_{LPJ})$ simulated by the LPJ-DGVM and the site observations, the yellow/blue indicating low/high correlation ; (b) ΔR^2 (correlation difference between GPP_{LAI} and GPP_{LPJ}), $BIAS(GPP_{LAI})$ and $\Delta ubRMSE(GPP_{LAI} - GPP_{LPJ})$;(c) ΔR^2 (correlation difference between GPP_{SMI} and GPP_{LPJ}) , $\Delta BIAS(GPP_{SMI})$ and $\Delta ubRMSE(GPP_{SMI} - GPP_{LPJ})$; (d) ΔR^2 (The correlation difference between GPP_{CO} and GPP_{LPJ}) , $\Delta BIAS(GPP_{CO})$ and $\Delta ubRMSE(GPP_{CO} - GPP_{LPJ})$, blue/red represent positive/negative values.

489

assimilation (scheme 3) for six sites representing six PFTs.

490

The residual analysis indicated that the three assimilation schemes for GPP (Figure S7 (left)) were

491

different. For the assimilation results, most of the errors were distributed around $-70 \sim 60 \text{ g C m}^{-2} \text{ month}^{-1}$

492

¹. The high GPP_{OBS} values were considerably underestimated. The maximum negative error reached 100

493

$\text{g C m}^{-2} \text{ month}^{-1}$. The error distribution of GPP_{SM} was more dispersed than that of GPP_{LAI} and GPP_{CO} .

494

Among the residuals of these three schemes, GPP_{SM} significantly overestimated the GPP_{OBS} , mainly

495

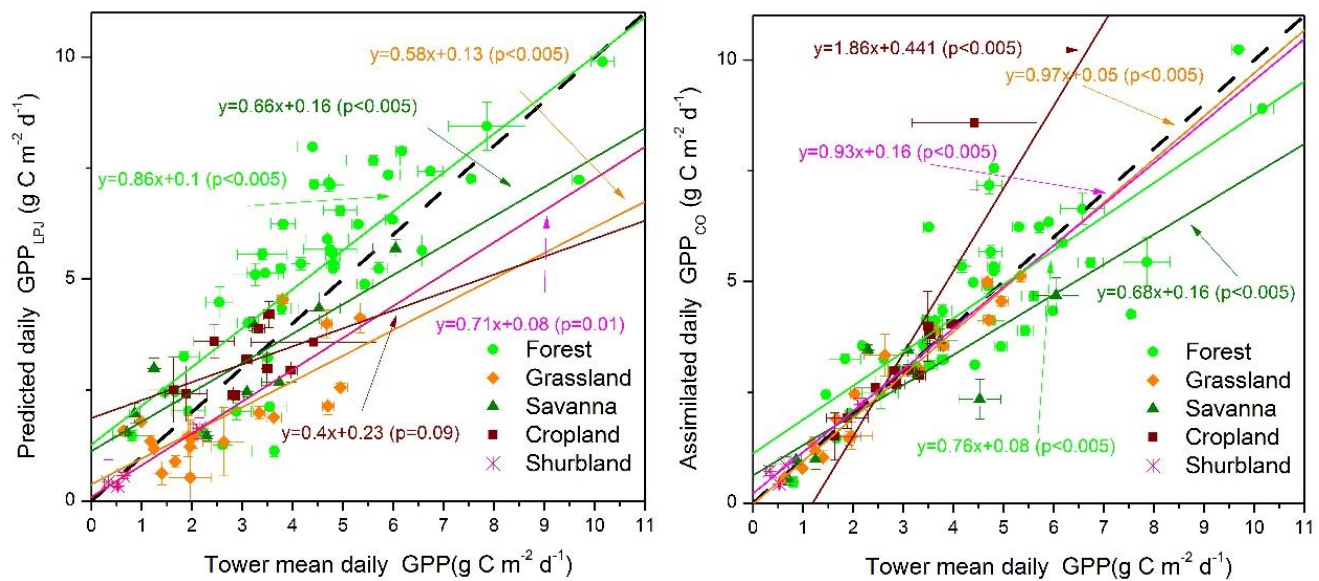
distributed in the $0\text{--}200 \text{ g C m}^{-2} \text{ month}^{-1}$ range. GPP_{LAI} showed significant improvement in the

496

overestimation of GPP_{OBS} compared with GPP_{CO} . In general, the GPP_{CO} with the most concentrated error

497

distribution had significant improvement.



498

499

Figure 4. Scatterplots of daily GPP_{LPJ} (left) and GPP_{CO} (right) versus tower GPP for different PFTs.

500

After determining the optimal assimilation scheme (scheme 3), we evaluated the GPP_{LPJ} and GPP_{CO}

501 at the site level (Fig.4). The results showed that GPP_{CO} performed better ($R^2= 0.83$, $\underline{ub}RMSD= 1.15$ g C
502 $m^{-2} d^{-1}$) than GPP_{LPJ} ($R^2= 0.69$, $\underline{ub}RMSD= \underline{2.15}1.91$ g C $m^{-2} d^{-1}$). The noticeable underestimation in all
503 PFTs and overestimation at most forest sites for GPP_{LPJ} were corrected by joint assimilation (GPP_{CO}).
504 Our joint assimilation methods had better performance in forests, shrublands, and grasslands than in
505 croplands and savannas. Except for the cropland, the linear fitting results of other types were all below
506 the 1:1 line, showing the overall underestimation. Superior performance in both original simulation and
507 assimilation occurred at shrubland ($R^2= 0.93$, $\underline{ub}RMSD= \underline{0.27}0.89$ g C $m^{-2} d^{-1}$) and grassland ($R^2= 0.97$,
508 $\underline{ub}RMSD= \underline{0.38}83$ g C $m^{-2} d^{-1}$) sites. However, the standard deviation of GPP_{CO} and GPP_{OBS} at savanna
509 sites was relatively large, and the assimilated GPP at several savanna sites was significantly
510 underestimated.

511 4.1.2 Accuracy assessment of ET for separate and ~~conjunct~~ joint assimilation

512 In general, the coefficient of determination (R^2) between ET_{LPJ} and ET_{OBS} was generally over 0.4
513 (the simulations were superior to GPP_{LPJ}) (Figure 5). ET_{LAI} showed slightly higher R^2 , while some sites
514 showed reduced values (41 sites). The ET_{SM} and ET_{CO} were significantly improved compared with the
515 ET_{LAI} . The R^2 increased considerably in Australia but declined at some sites in the United States after
516 assimilation. For ~~RMSD and~~ $\underline{ub}RMSD$, ET_{CO} performed better than ET_{SM} and ET_{LAI} . The SM
517 assimilation improved more in humid regions, while ~~the RMSD of ET_{LAI} only slightly improved in~~
518 ~~Australia and~~ the $\underline{ub}RMSD$ of ET_{SM} was slightly higher in South America. ~~According to the bar chart~~
519 ~~(Fig.5-RMSD(b)), the LAI assimilation increased the ET simulation error.~~ In the original LPJ-DGVM

520 simulation, the sites with a negative bias were mostly located in the humid and dry-sub humid regions,
521 while most of the sites in arid and semi-arid regions had underestimation (Fig. 5-BIAS(a), Table S3).
522 The assimilation improved ET at some of the overestimated sites, but the underestimation over these
523 sites showed little improvement.

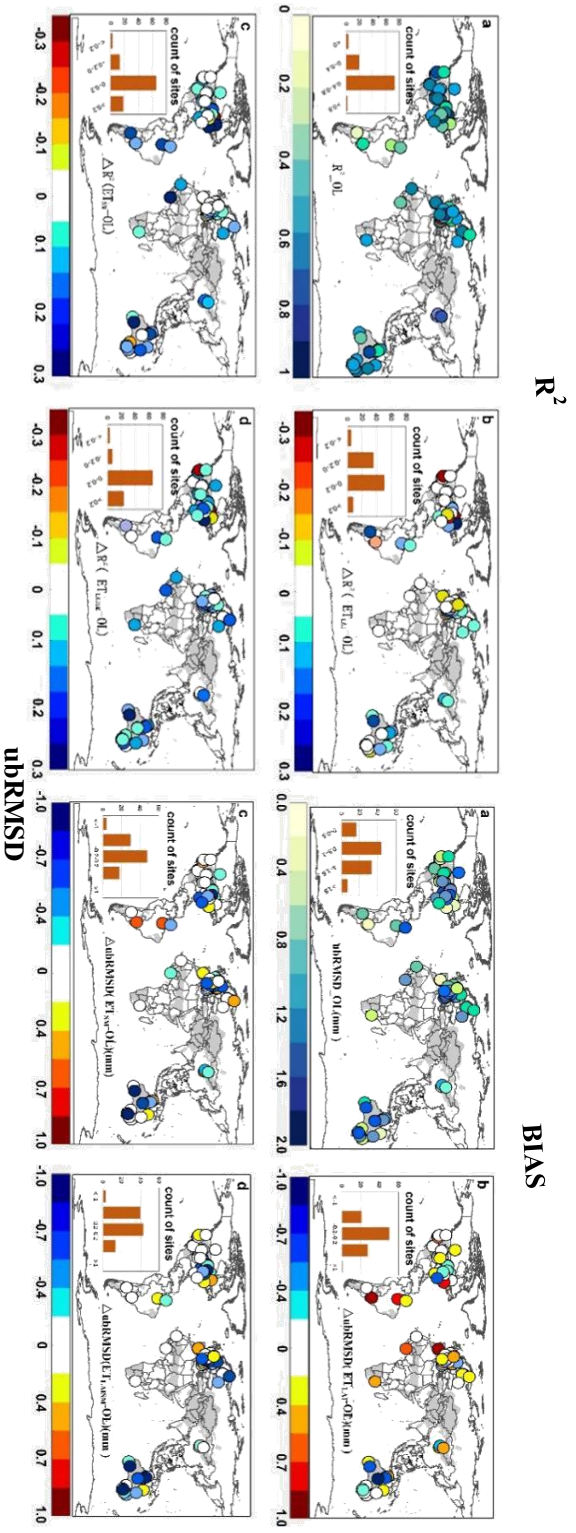


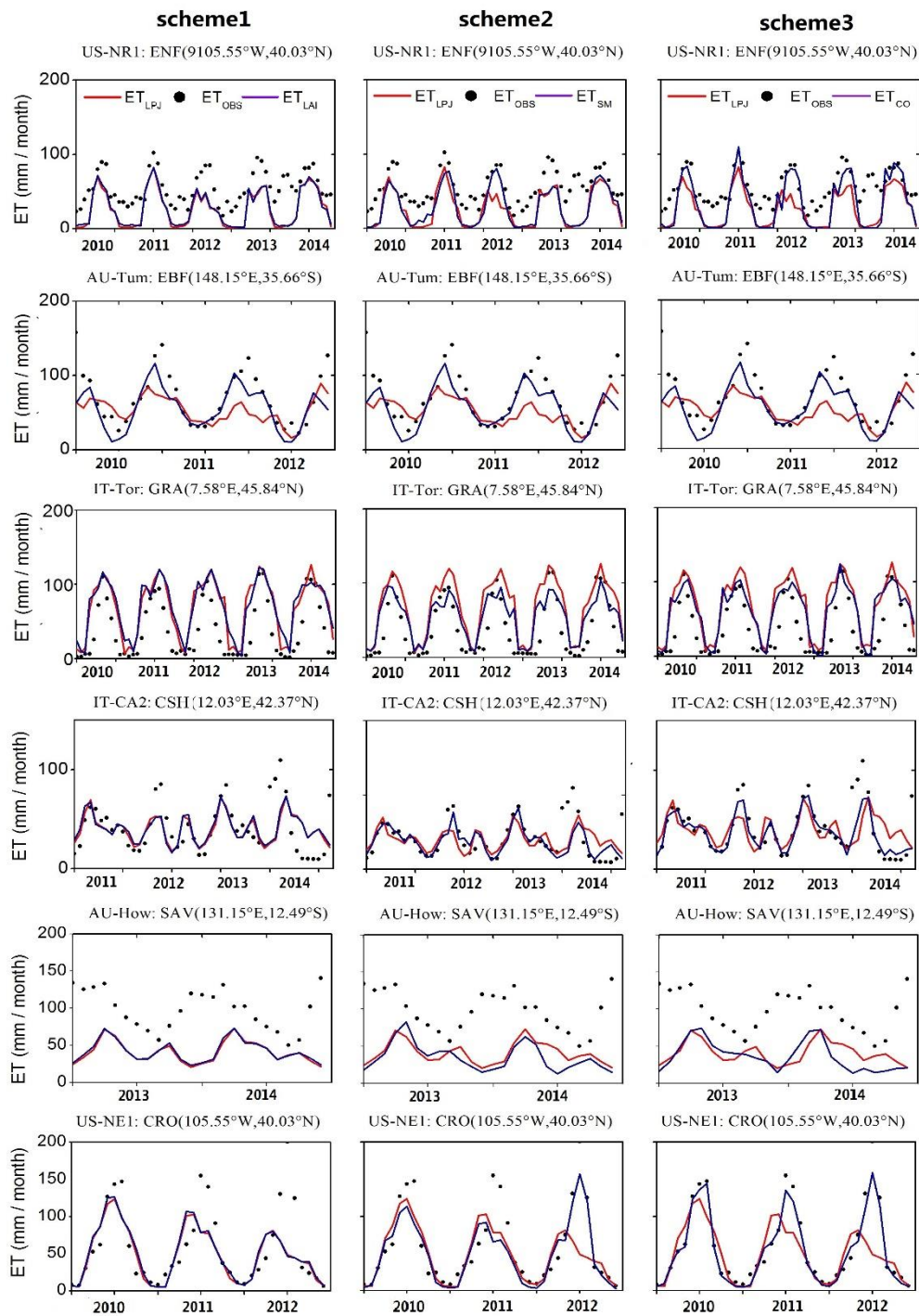
Figure 5 (a) The correlation coefficient, BIAS and the Unbiased Root Mean Square Error (ubRMSSE) between the $ET_{GPP_{LPJ}}$ simulated by the LPJ-DGVM and the site observations, with yellow/blue indicating low/high correlation or ubRMSSE; (b) ΔR^2 (correlation difference between ET_{SM} and ET_{LPJ}), BIAS (ET_{SM}) and Δ ubRMSD ($ET_{SM} - ET_{LPJ}$); (c) ΔR^2 (correlation difference between ET_{CO} and ET_{LPJ}), BIAS (ET_{CO}) and Δ ubRMSD ($ET_{CO} - ET_{LPJ}$), blue/red represent positive/negative value.

525 At the seasonal scale, the model simulations were able to capture the temporal trend of ET_{OBS} , and
526 joint assimilation significantly improved the simulation in the growing season (US-NR1, US-NE1);
527 overall underestimation was observed for ET_{OBS} , especially in winter (Figure Fig-6). Overall, the linear
528 fitting of monthly ET_{CO} and ET_{OBS} was closer to 1:1 than that of ET_{LAI} and ET_{SM} (Figure S6). The
529 simulation accuracy of joint assimilation was better than that of separate assimilation, and the
530 performance of the SM assimilation was better than that of the LAI assimilation.

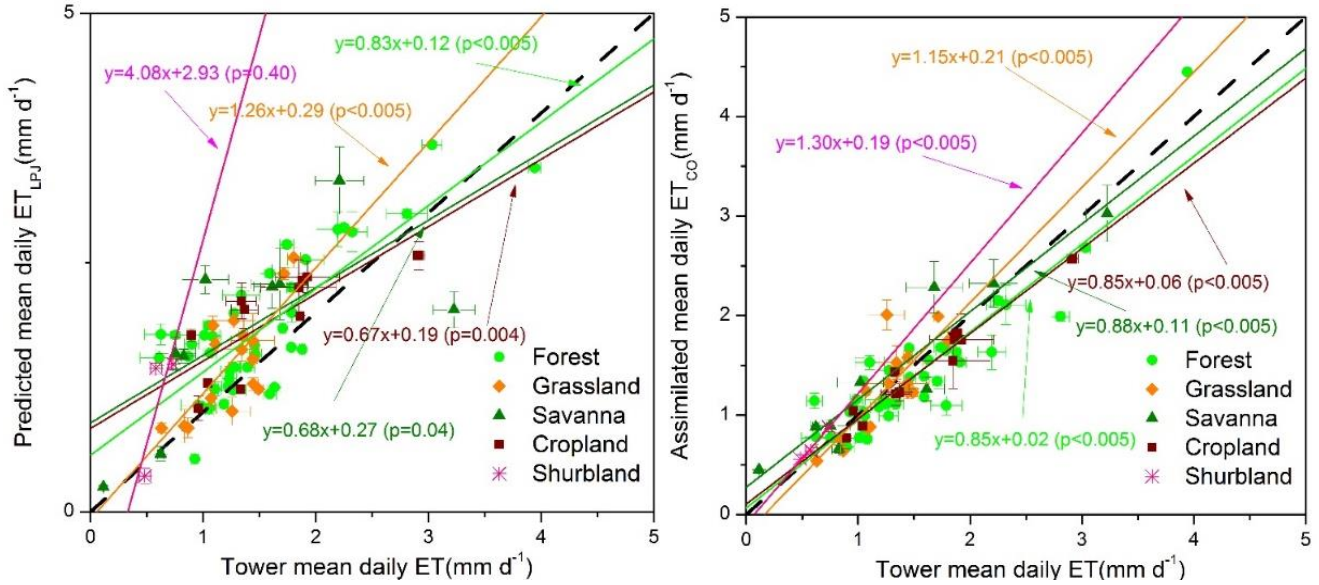
531 The ET residual analysis (Figure S7 (right)) indicated that the three assimilation scheme errors
532 showed underestimation for ET_{OBS} . In general, the error distribution of separate assimilations was more
533 dispersed than that of the joint assimilation. Similar to the assimilation performance of GPP, ET_{CO} and
534 ET_{SM} significantly improved the overestimation of ET_{OBS} , but did not significantly improve the
535 underestimation. For the ET_{CO} , most of the errors were distributed around -30–18 mm month⁻¹. The region
536 with high ET_{OBS} was considerably underestimated, and the maximum negative error reached -57 mm
537 month⁻¹.

538 We also evaluated the ET assimilation results at the PFT scale (Figure 7). The results showed that
539 our assimilated ET performed better at the site level ($R^2= 0.77$, ubRMSD= 0.28-65 mm d⁻¹) than that of
540 ET_{LPJ} ($R^2= 0.67$, ubRMSD=0.98-95 mm d⁻¹). Joint assimilation significantly reduced the errors of those
541 shrubland sites with overestimation for ET_{OBS} , and the site distribution was closer to the 1:1 line. Our
542 assimilation methods had better performance in forest, savanna, and grassland ecosystems than in
543 cropland and shrubland (Table S3). The linear fitting results of grassland and shrubland were all above
544 the 1:1 line, showing overall overestimation. Although the original simulation and assimilation
545 performance were superior at savanna sites ($R^2= 0.95$, ubRMSD= 0.33-78 mm d⁻¹), the standard

546 deviations of ET_{CO} and ET_{OBS} at savanna sites were relatively large, which was similar to the GPP results
547 at savanna sites.



549 **Figure 6. Seasonal cycles of tower-based and simulated ET from Lund-Potsdam-Jena (LPJ), GLASS LAI**
 550 **assimilation (scheme 1), SMOS assimilation (scheme 2) and joint assimilation (scheme 3) for the six sites**
 551 **representing six PFTs during the study period.**

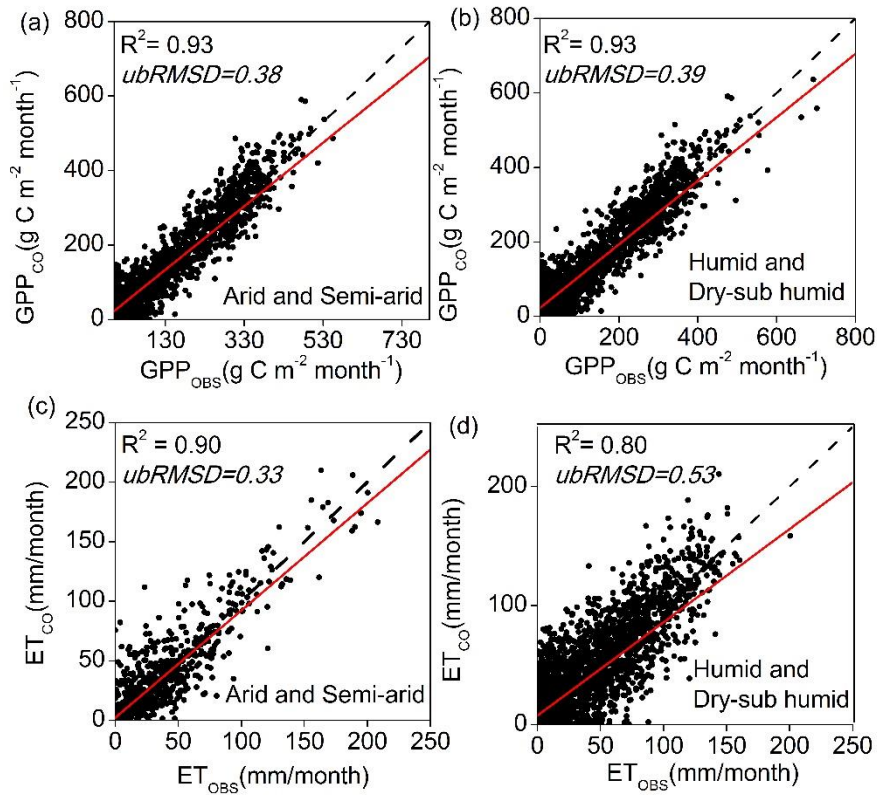


552

553

Figure 7. Scatter plots of daily ET_{CO} versus tower ET under different PFTs.

554 *4.2. Comparison of assimilation performance in semi-arid and arid regions with that in humid and dry-*
 555 *sub humid regions*



556

557

558

559

Figure 8. Scatter plots of daily tower GPP and ET versus GPP_{CO} and ET_{CO} under different arid and humid sites: (a) and (c) are the fitting results of GPP and ET in arid and semi-arid regions, respectively; (b) and (d) are the fitting results of GPP and ET in humid and dry sub-humid zone, respectively.

560

561

562

563

564

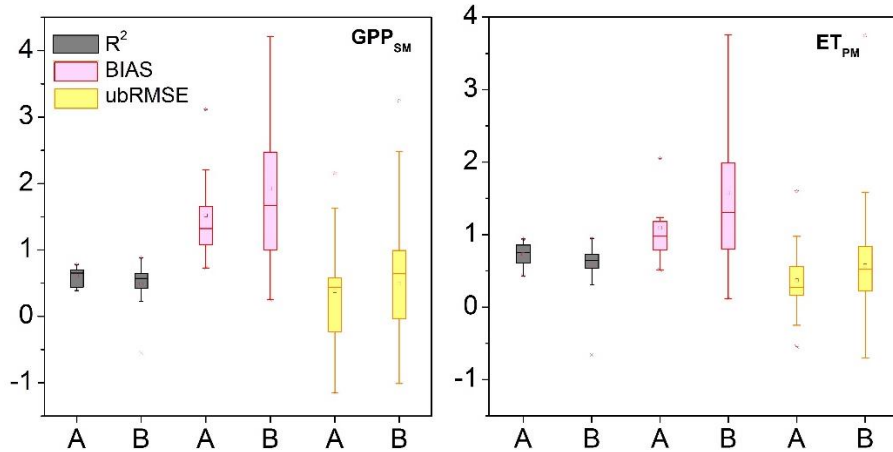
During the period 2010–2014, monthly GPP_{CO} and ET_{CO} performed differently in humid and sub-dry humid regions and semi-arid and arid regions (Figure 8, Table S2,3). Overall, the GPP and ET simulations had good consistency with the tower data in the two regions. For GPP_{CO} , there was no significant difference in the correlation and fitting coefficients between the two regions. ~~Due to the higher standard deviation and GPP_{OBS} values in the humid and sub-dry humid regions than in the semi-~~

565 ~~arid and arid regions, the higher RMSD of the humid and sub-dry humid regions did not reflect higher~~
566 ~~accuracy in semi-arid and arid regions.~~ As for ET_{CO} , the fitting results and R^2 values in the semi-arid
567 and arid regions performed better than those in the humid and sub-dry humid regions, which also
568 suggested the importance of surface SM for ET estimation in water-limited areas.

569 On the daily scale, the original GPP simulations (GPP_{LPJ}) performed better in the semi-arid and
570 arid regions than in the humid and sub-dry humid regions with higher R^2 and lower ubRMSD (Table S2).
571 the R^2 and bias implied that the LAI assimilation alone had a better performance than the SM assimilation
572 alone. However, for sites in arid and semi-arid areas, the RMSD and ubRMSD showed that the GPP_{SM}
573 improved better than GPP_{LAI} , which both demonstrated SM data are essential in water-limited regions.
574 For GPP_{CO} , the shrubland in the semi-arid and arid regions had the lowest R^2 values and the second lowest
575 ubRMSD. The forest in the semi-arid and arid regions had the largest improvement after assimilation. In
576 the humid and sub-dry humid regions, the GPP_{CO} of the savanna and cropland showed the largest
577 improvement (R^2 increased by 64.7% and 71.1%, respectively; ubRMSD decreased by 47.0% and 31.8%,
578 respectively). The grassland in the semi-arid and arid regions had the highest R^2 , and the savanna by
579 combining all indicators had the best assimilation results compared to other types in both regions.

580 Similar to ET_{CO} , the ET_{LPJ} in the semi-arid and arid regions was better than that in humid and sub-
581 dry humid regions in terms of four evaluation indicators (~~RMSD decreased by 32.7%, ubRMSD decreased~~
582 ~~by 34.4% in semi-arid and arid regions and RMSD decreased by 26.4%, and the ubRMSD decreased by~~
583 30.9% in humid and sub-dry humid regions compared with ET_{LPJ}). The R^2 and ubRMSD implied that the
584 SM assimilation alone had a better performance than the LAI assimilation alone, especially for sites in

585 arid areas. and the bias showed that the ET_{LAI} improved better than ET_{SM} for sites in humid and sub-dry
 586 humid areas. The performance of the original simulation and assimilation of grassland sites in the semi-
 587 arid and arid regions was the best among all five PFTs.

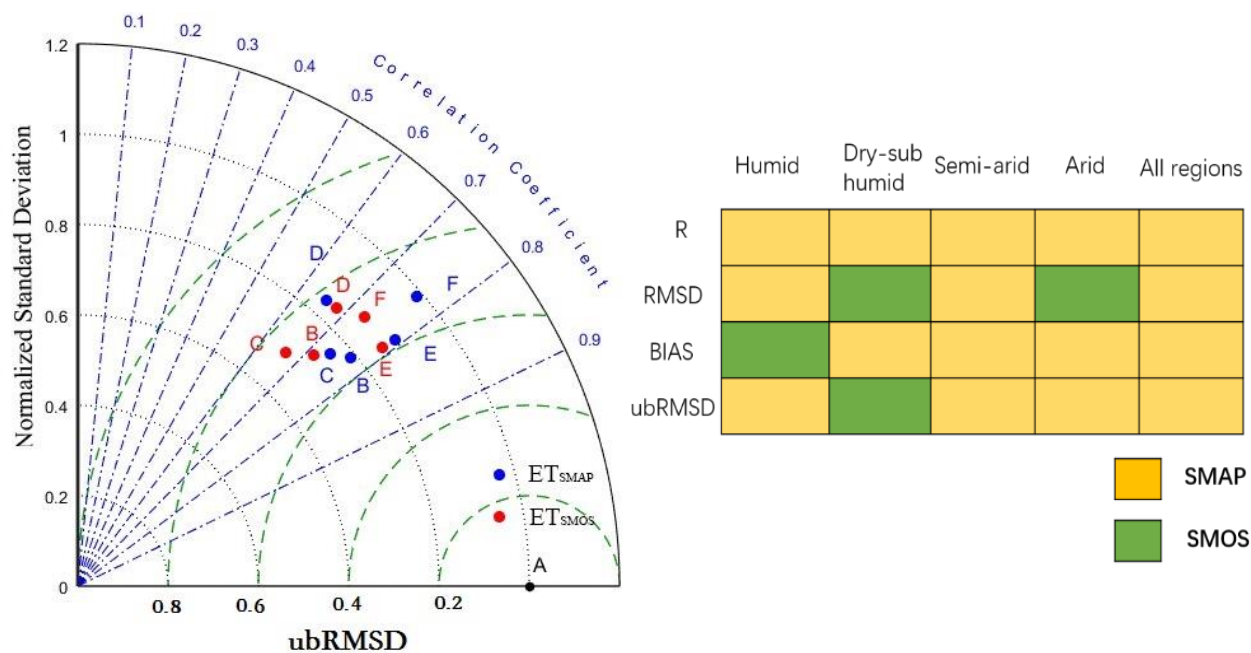


589
 590 **Figure 9. Boxplots of R^2 , ubRMSD and BIAS for GPP_{SM} (left) and ET_{PM} (right). A represents the sites in arid**
 591 **and semi-arid areas, and B represents the sites in humid and dry sub-humid areas.**

592 To investigate the reasons for better assimilation performance in water-limited regions, we evaluated
 593 the GPP and ET simulated by the LPJ-PM according to R^2 , ubRMSD, ~~RMSD~~, and BIAS (Figure 7).
 594 Compared with the semi-arid and arid regions, the humid and sub-dry humid region had smaller R^2 mean,
 595 larger BIAS ~~and RMSD mean~~, and no significant difference in mean ubRMSD for GPP_{SM} . In general, the
 596 evaluation results of joint assimilation for ET_{PM} were generally consistent with those for GPP_{SM} and
 597 GPP_{SM} . ET_{PM} showed underestimation, which was consistent with the underestimation in SM assimilation.

598 These results indicated that, both GPP and ET modeled by LPJ-PM with joint assimilation were less stable
 599 and had a lower performance in the humid and sub-dry regions than in the semi-arid and arid regions.

600 *4.3. Comparison of assimilation performance in assimilating SMOS and SMAP soil moisture data*



A:Reference point B: Cropland C: Shrubland D: Forest E: Grassland F: Savanna

601

602 **Figure 10. Taylor diagram (left) comparing ET simulations with observations at all 46 AmeriFlux sites at**
 603 **the daily time step between April 2015 and December 2018. Blue dots represent results based on**
 604 **assimilation with SMAP SM only and red dots represent results based on assimilation with SMOS SM**
 605 **only. Reference points A and B-F correspond to the vegetation functional types (PFTs). The grid diagram**
 606 **(right) compares the evaluation indices of ET simulations with those of the observed values at all 46**
 607 **AmeriFlux sites with different wet and dry zones at the daily time step; the yellow cells indicate that**
 608 **ET_{SMAP} performs better in the metric, and green cells indicate that ET_{SMOS} performs better in the metric.**

609 The Taylor chart was used to compare the assimilation performance of ET_{SMAP} and ET_{SMOS} at 46
610 AmeriFux sites (Figure 10-left). The results showed that ET_{SMAP} performed better than ET_{SMOS} for all
611 PFTs. Both ET_{SMAP} and ET_{SMOS} performed well for grassland (closer to point A), and there was little
612 difference between R^2 and standardized RMSD. The NSD of ET_{SMAP} in grassland was 0.88, which was
613 closer to 1 than that of ET_{SMOS} . The assimilation of ET in the forest had a lower R and higher standardized
614 RMSD (0.7-0.8) than those of other PFTs, and the NSD of cropland and shrubland was lower than that of
615 other PFTs (0.6-0.8), indicating that the assimilation for cropland and shrubland could not reproduce the
616 variations in ET effectively. However, ET_{SMAP} showed significant improvement in R^2 compared with
617 ET_{SMOS} for shrubland and cropland. The assimilation performance of ET_{SMAP} and ET_{SMOS} for savanna
618 showed the greatest difference. In general, the ET_{SMAP} and ET_{SMOS} were slightly different, and the ET_{SMAP}
619 was more improved than ET_{SMOS} .

620 Figure 10 (right) shows the assimilation accuracy of ET_{SMOS} and ET_{SMAP} in different humid and arid
621 regions. The ET_{SMAP} had significant advantages for the four indicators. The R of ET_{SMAP} was higher than
622 that of ET_{SMOS} in all the areas. However, ET_{SMOS} in some evaluation indicators showed a better
623 performance than ET_{SMAP} (BIAS in the humid region; ~~RMSD and~~ ubRMSD in the sub-dry humid region).
624 This may be due to the overall more humid nature of SMOS SM than the SMAP SM. Moreover, the
625 sensitivity of deep soil moisture contributed more to the ET in humid areas than in the water-limited areas.

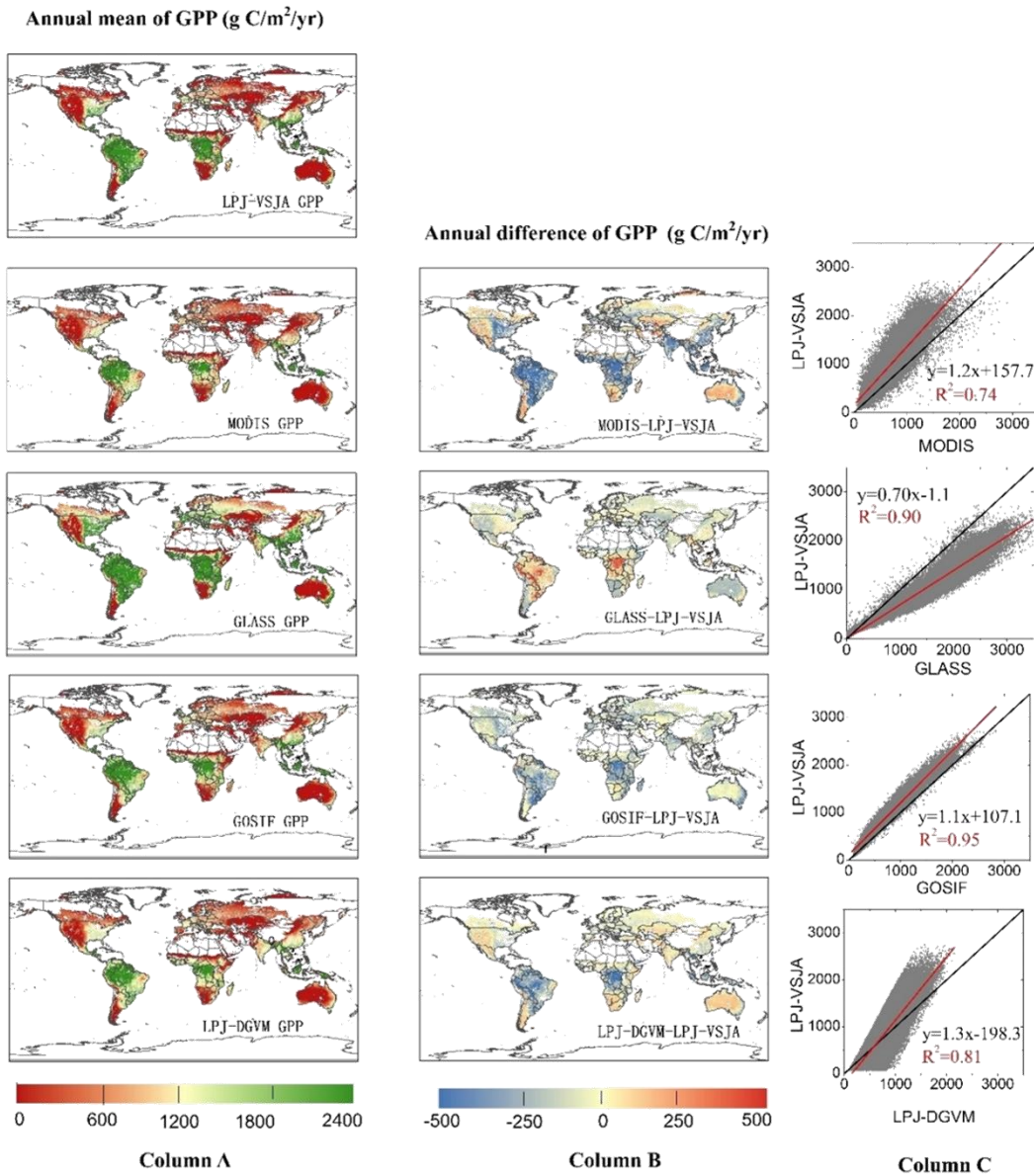
626 4.4. Global simulations of GPP and ET with joint assimilation of LAI and soil moisture data

627 To assess the spatial scalability of the LPJ-VSJA assimilation scheme, we simulated the global daily
628 GPP and ET for 2010–2018 with a spatial resolution of 0.25° . The original results simulated by the LPJ-

629 DGVM and LPJ-VSJA were referred to as LPJ-DGVM GPP(ET) and LPJ-VSJA GPP(ET), respectively.
630 We compared the annual spatial GPP and ET values and the error standard deviation of the LPJ-VSJA
631 with several existing flux products.

632 Figures 11 and 12 depict the spatial distribution of the annual mean and the differences between our
633 simulation results and the global independent satellite-based products. The developed LPJ-VSJA GPP
634 was the closest to GOSIF GPP (Li and Xiao 2019) in most regions with the lowest spatial mean deviation
635 (LPJ-VSJA-GOSIF) ($27.9 \text{ g C m}^{-2} \text{ yr}^{-1}$), followed by GLASS GPP ($51.2 \text{ g C m}^{-2} \text{ yr}^{-1}$) (Yuan et al. 2010),
636 LPJ-DGVM ($-73.4 \text{ g C m}^{-2} \text{ yr}^{-1}$), and MODIS GPP ($93.1 \text{ g C m}^{-2} \text{ yr}^{-1}$). LPJ-VSJA had higher GPP values
637 than GOSIF GPP in tropical regions, such as Amazonia, Central Africa, and Southeast Asia. In general,
638 the annual mean and differences between MODIS, GOSIF GPP, LPJ-DGVM, and our LPJ-VSJA were
639 in broad agreement (with higher R^2 ranging from 0.74 to 0.95).

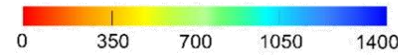
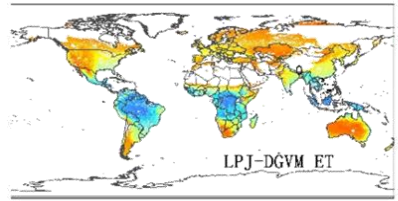
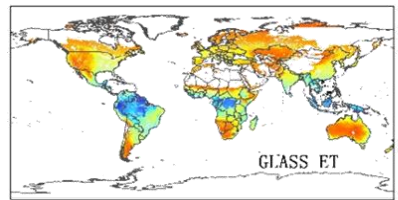
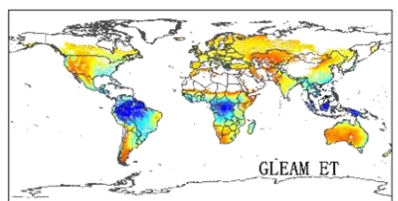
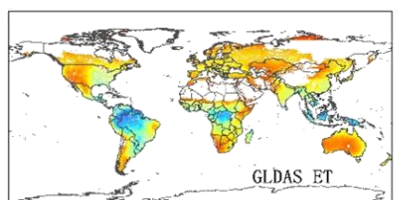
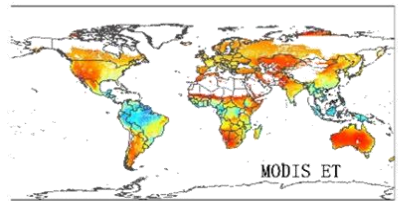
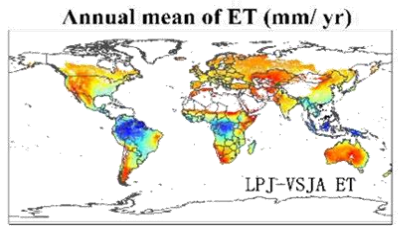
640 LPJ-VSJA ET was the closest to GLEAM ET on the spatial average with the least spatial average
641 deviation (-13.9 mm yr^{-1}) and highest R^2 (0.88), followed by GLASS ET (-23.1 mm yr^{-1} and 0.82), GLDAS
642 ET (-34.7 mm yr^{-1} and 0.73), LPJ-DGVM (-48.7 and 0.66 mm yr^{-1}), and MODIS ET (-122.1 and 0.54 mm
643 yr^{-1}).



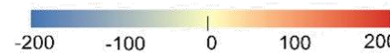
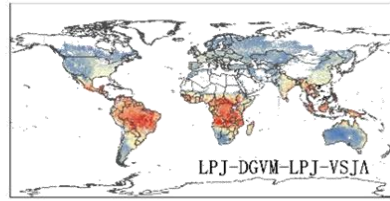
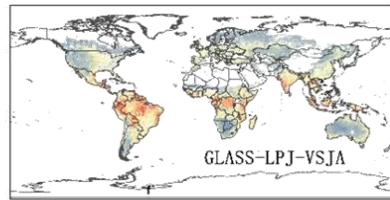
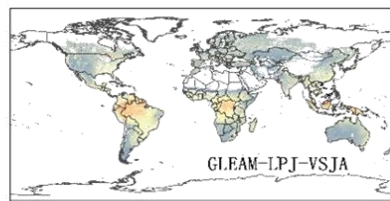
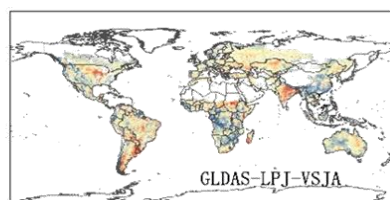
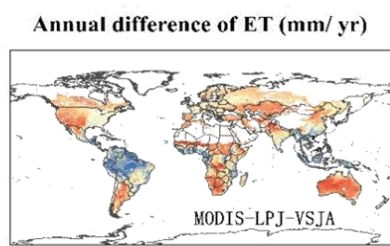
644

645 **Figure 11. Column A: Spatial distribution of annual LPJ-VSJA GPP and other independent satellite-based**
 646 **datasets (a: MODIS GPP; b: GLASS GPP; c: GOSIF GPP; e: LPJ-DGVM). Column B: Spatial**
 647 **distribution of the difference between annual LPJ-VSJA GPP and other independent satellite-based**

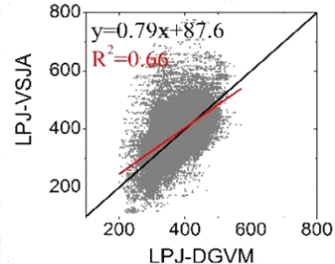
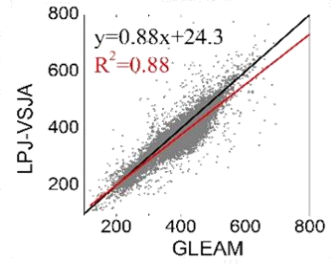
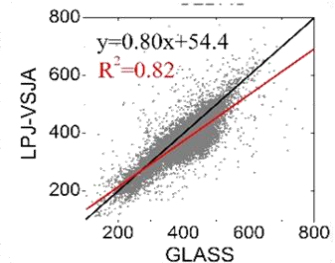
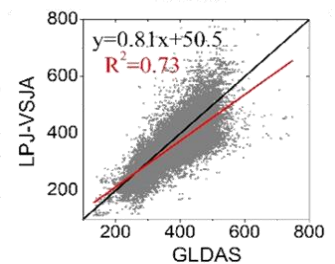
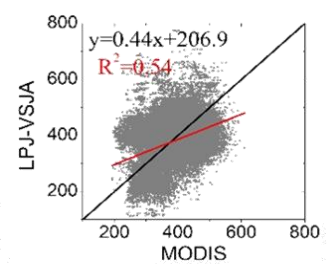
648 **datasets. Column C: Scatter plots between these products. Black lines show the 1:1-line, red lines show the**
649 **regression fit.**



Column A



Column B



Column C

651 **Figure 12. Column A: Spatial distribution of annual LPJ-VSJA ET and other independent satellite-**
652 **based datasets (a: MODIS GPP; b: GLDAS ET; c: GLEAM ET; d: GLASS ET; e: LPJ-DGVM ET).**
653 **Column B: Spatial distribution of the difference between annual LPJ-VSJA ET and other independent**
654 **satellite-based datasets. Column C: Scatter plots between these products are provided on the right of the**
655 **difference maps. Black lines show the 1:1-line, red lines show the regression fit.**
656

657 Figure 13 (a)–(e) represent the spatial error standard deviation (σ) distribution of MODIS, GLASS,
658 GOSIF, and LPJ-VSJA GPP, respectively. The graphs on the right side depict the corresponding
659 histograms. The σ of the MODIS GPP was evenly distributed between 30 and 60 g C m⁻² month⁻¹
660 g C/m²/month, while the average σ of other products was concentrated in 0–20 g C m⁻² month⁻¹ (90%). The
661 high errors of all products were concentrated in the high temperature and humid areas of southern North
662 America, eastern South America, humid and dry sub-humid areas of South Asia, and the savannas of
663 Africa and Australia. The error histogram of GOSIF GPP and LPJ-DGVM GPP were in line with the
664 normal distribution, with an average value of 8.3 g C m⁻² month⁻¹ and 22.4 g C m⁻² month⁻¹. The GLASS
665 GPP product had the lowest mean value (3.6 g C m⁻² month⁻¹), followed by LPJ-VSJA (4.7 g C m⁻² month⁻¹),
666 but the error variance of the LPJ-VSJA product was the lowest, indicating a stability of the regional
667 error (Table S4). Compared to the LPJ-DGVM, the joint assimilation results showed improvement in all
668 regions (the average error reduced by 17.7 g C m⁻² month⁻¹), especially in the humid regions of South
669 Asia, Australia, and the United States. Our LPJ-VSJA GPP was generally proven to have high accuracy
670 and stability for spatial analysis and could provide a reference for other model products.

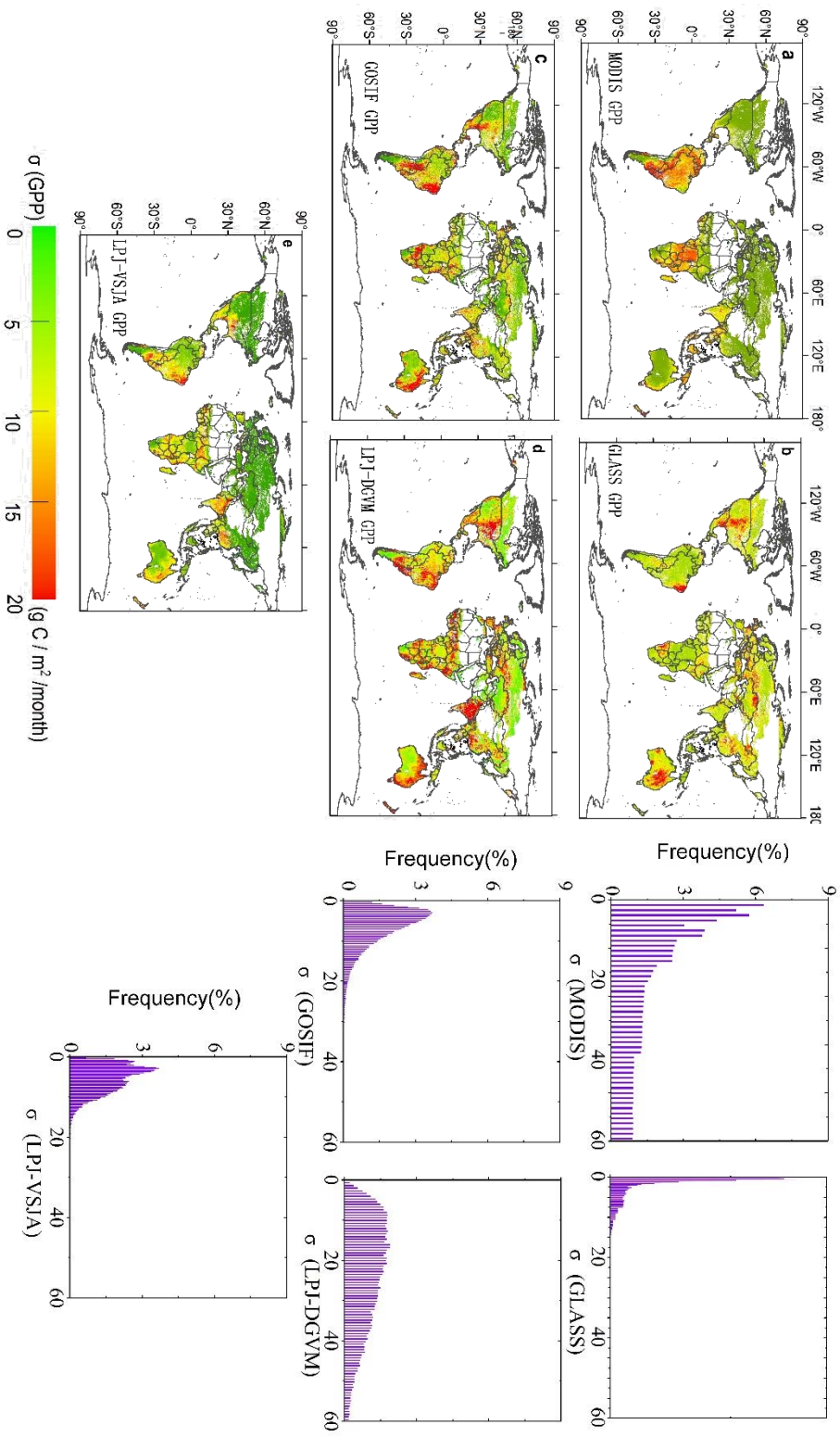


Figure 13. Spatial distribution and histograms of error standard deviation (σ) for global GPP products:

MODIS (a), GOSIF (b), GLASS (c), LPJ-DGVM (d), and LPJ-VSJA (e).

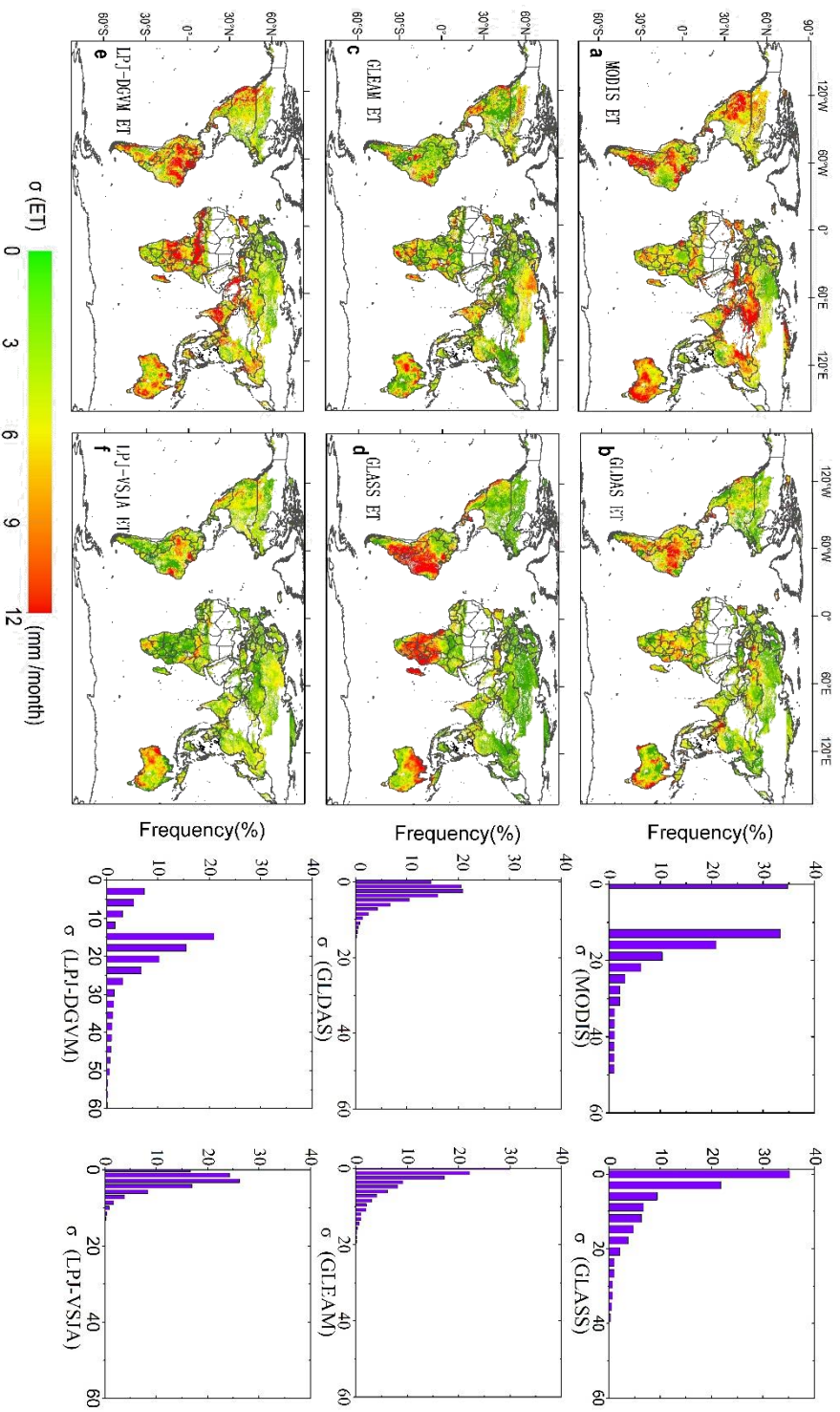


Figure 4. Spatial distribution and histograms of error standard deviation (σ) for global ET products:

MODIS (a),GLDAS (b),GLEAM (c), GLASS (d), LPJ-DGVM (e), and LPJ-VSJA (f).

673 Figures 14 (a)–(f) show the σ of MODIS, GLDAS, GLEAM, GLASS, and LPJ-VSJA ET (the units
674 are mm/month), and the right graphs are the corresponding histograms. The σ values of GLDAS and LPJ-
675 VSJA represented a normal distribution trend. Except for MODIS, GLASS, and LPJ-DGVM (0–60 mm
676 month⁻¹), the σ of other products was generally between 0-20 mm month⁻¹. The simulation error was
677 relatively smaller in the Northern Hemisphere than in the Southern Hemisphere, especially for GLASS
678 ET and GLDAS ET. Significant improvements in joint assimilation were observed in the northern
679 hemisphere (especially in the semi-arid areas of the western United States and savanna and cropland areas
680 of central India) and African savanna areas, and the average error was reduced by 15.1 mm month⁻¹. In
681 general, the error mean and variance of LPJ-VSJA and GLEAM products were relatively low (Table S4),
682 and there was no apparent extremely high value region in the error distribution. Among the five products,
683 LPJ-VSJA had the lowest error mean and variance and the highest accuracy.

684 5. Discussion

685 5.1 Advantage of joint assimilation for GPP and ET

686 The benefit of employing multiple data flows in an assimilation system is the complementarity of
687 the data, which enables constraints on different components of the underlying process-based terrestrial
688 biosphere model. Due to the interaction and feedback between the internal components of the model, the
689 assimilation of multiple observations has a synergistic effect, and the integrated constraints are greater
690 than the individual constraint (Kato et al. (2013)). The advantage of our joint assimilation is that it can
691 improve the simulation accuracy of both GPP and ET, especially ET, in arid and semi-arid regions.

692 In the GPP assimilation experiment, the performance of the LAI assimilation was better than that of
693 the SSM assimilation possibly for two reasons: (1) the LPJ-VSJA is more controlled by LAI data because
694 the ratio of assimilated LAI (daily input) to SSM observations (3-day interval input) is approximately 3:1,
695 which makes the likelihood function biased to LAI data; (2) the SM directly influences the simulation of
696 ET, and the corresponding time function (computes the top layer SM (50 cm)) used here by Zhao et al.
697 (2013)(section 2.4) will result in the error of the updated top SM and propagating the error to the GPP_{SM}.
698 ~~Moreover, GPP is not only directly affected by LAI but also by other vegetation and environmental~~
699 ~~conditions. These multiple dependencies (direct and indirect) make GPP less likely to respond to transient~~
700 ~~changes in LAI (Zobitz et al. 2014). In addition, the LAI dynamic variability varies depending on the~~
701 ~~ecosystem type. For instance, the LAI for coniferous forest has less dynamic variability than for cropland~~
702 ~~and the deciduous forest (Turner et al. 2006; Turner et al. 2005).~~, the 8-day interval LAI has the capability

703 to capture the temporal variability of phenology. ~~The LAI assimilation with different time scales (e.g.,~~
704 ~~8 day interval, monthly, annual) for different ecosystems may achieve better results.~~

705 Current studies on terrestrial water and carbon flux assimilation mostly focus on the assimilation
706 between a single model framework and observation results, lacking the fusion and comparison between
707 multiple models. The processed models used in DA are simplifications and approximations of reality, and
708 different models focus on different ecological processes. In this study, the updated ET module was
709 integrated to compensate for the simplification of soil stratification and the lack of SM information in the
710 hydrological module of the LPJ-DGVM. Therefore, the integration of multiple types of models and multi-
711 source observation data (remotely sensed data, ecological inventory data (National Ecological
712 Observatory Network, NEON (Keller et al. 2008)), and other measurements (Desai et al. 2011; Hayes et
713 al. 2012) is expected to more objectively and effectively simulate the real state of ecosystems.

714 *5.2 Comparison of joint assimilation (LPJ-VSJA) and other models for GPP and ET across regions and* 715 *vegetation types*

716 Global GPP and ET for different products were calculated by multiplying the global mean GPP
717 density flux with the global vegetation area (122.4 million km²) originated from the MODIS land cover
718 product (Friedl et al. 2010). The mean global GPP of the LPJ-VSJA (130.2 Pg C yr⁻¹) was
719 approximately 12% lower than that of PML-V2 (145.8 Pg C yr⁻¹) and 18% higher than that of GLASS
720 and MODIS, respectively (Table S6). The GPP values of LPJ-VSJA and GOSIF were the most similar.
721 The GOSIF GPP was developed from gridded SIF using simple linear relationships between SIF and

722 GPP. Our global LPJ-VSJA GPP estimates were within the currently most plausible 110–150 Pg C/yr
723 range.

724 As for ET, our results were similar to those of GLEAM ET and lower than those of PML-V2,
725 GLDAS-2, and GLASS ET (~ 72000 mm yr⁻¹). Joint assimilation improved the overestimation of LPJ-
726 DGVM ET. At the daily scale, the estimation accuracy of PML-V2 and GLDAS-2 products, calibrated
727 with flux tower data, was better than that of our estimates, which suggests an underestimation of LPJ-
728 VSJA ET in wet regions. It is likely because the SM of SMAP or SMOS was underestimated in the wet
729 region or the influence of deep SM was under-represented. According to Seneviratne et al. (2010),
730 satellite-based ET estimation approaches often overestimate ET in areas of arid and semi-arid climatic
731 regimes in the magnitude of 0.50 to 3.00 mm d⁻¹. The poor performance of these models can largely be
732 attributed to the lack of constraints of SM and more accurate vegetation parameters (Gokmen et al. 2012;
733 Pardo et al. 2014). For instance, the monthly estimated ET modeled by the Penman-Monteith-Leuning
734 (PML) model agreed with flux tower data well ($R^2 = 0.77$; bias = -9.7% , approximately 0.2 mm d⁻¹).
735 Our annual ET simulations were lower than other products and slightly underestimated tower ET with a
736 bias of 0.19 mm d⁻¹ ($ET_{OBS} - ET_{CO}$).

737 In general, GPP and ET had better assimilation performance in arid and semi-arid regions than in
738 humid and semi-humid regions likely because of the following reasons. First, the incorporation of surface
739 SM is more important for vegetation growth in water-limited areas. The module PT-JPL_{SM} has been
740 proven to have better performance in semi-arid and arid regions (Purdy et al. 2018). Our integrated model
741 LPJ-PM also performed better in semi-arid and arid regions by assimilating SMAP soil moisture (Li et al.

742 2020). Second, the input performance, including SMOS and SMAP SM products, is better in arid and
743 temperate regions than in cold and humid regions (Zhang et al. 2019). Third, the vegetation types in humid
744 regions are more complex and relatively less accurately simulated by the LPJ-DGVM within a single grid
745 cell. For comparison, Zhang et al. (2020) used a data-driven upscaling approach to estimate GPP and ET
746 in global semi-arid regions. This data-driven approach ($R^2 = 0.79$, $\text{RMSD} = 1.13 \text{ g C m}^{-2} \text{ d}^{-1}$) had slightly
747 higher performance in estimating GPP than our LPJ-VSJA ($R^2 = 0.73$ and $\text{RMSD} = 1.14 \text{ g C m}^{-2} \text{ d}^{-1}$) ~~and~~;
748 the data-driven method ($R^2 = 0.72$ and $\text{RMSD} = 0.72 \text{ mm d}^{-1}$) had identical performance for estimating
749 ET with our LPJ-VSJA ($R^2 = 0.73$ and $\text{RMSD} = 0.72 \text{ mm d}^{-1}$).

750 Our assimilation performance varied with PFT. The GPP and ET assimilation results of savanna sites
751 performed well in both dry and wet regions, and those of shrubland sites showed the most remarkable
752 improvement for simulations of LPJ-DGVM. The original simulation and assimilation performance of
753 grassland sites in the semi-arid and arid regions were the best for all five PFTs. Consistent with our
754 research, previous studies also showed better GPP or ET simulations for grassland, savannas, and
755 shrublands biomes. For instance, Feng et al. (2015) validated five satellite-based ET algorithms for semi-
756 arid ecosystems and concluded that all the models produced acceptable and relatively better results for
757 most grassland, savanna, and shrubland sites. Yang et al. (2017) demonstrated that the GLEAM ET had a
758 superior performance for the grassland sites. The GOSIF GPP demonstrated better simulation for
759 grassland and woody savannas sites at 8-day time steps with higher R^2 (0.77 and 0.83, respectively) and
760 lower RMSD ($1.48 \text{ g C m}^{-2} \text{ d}^{-1}$ and $1.1 \text{ g C m}^{-2} \text{ d}^{-1}$) (Li and Xiao 2019). In contrast, our LPJ-VSJA GPP

761 showed an R^2 of 0.87 for grassland and 0.75 for savannas and an RMSD of $1.11 \text{ g C m}^{-2} \text{ d}^{-1}$ and 1.1 g C
762 $\text{m}^{-2} \text{ d}^{-1}$, respectively, in semi-arid and arid regions.

763 *5.3 Uncertainty analysis of joint assimilation*

764 Our validation results at both site and regional scales indicated that uncertainty existed in LPJ-VSJA
765 daily GPP and ET estimates. The errors from the tower EC observations, model-driven data, model
766 structure, error of satellite-based observations (e.g., LAI and SM), and the spatial scale mismatch between
767 the ground observed footprint size and satellite-derived footprint size were the vital factors affecting
768 assimilation performance.

769 First, recent studies have revealed errors in the GLASS LAI and SMOS or SMAP SM compared
770 with ground measurements. By computing the RMSD and R^2 of each product, the GLASS LAI accuracy
771 was clearly superior to that of MODIS and Four-Scale Geometric Optical Model based LAI (FSGOM) in
772 forests and GLASS and FSGOM led to in much higher annual GPP and ET estimates compared to
773 MCD15(Liu et al. 2018). The vegetation type (or land cover) misclassification caused 15–50% differences
774 in LAI retrieval (Fang and Liang 2005; Gonsamo and Chen 2011). Yan et al. (2016) calculated a RMSD
775 of 0.18 for the GLASS LAI over a range of HeiHe drainage basin sites and used the error to improve the
776 simulation of LAI and fluxes by assimilating GLASS LAI data. Previous studies reported an improvement
777 in the performance of the SMOS and SMAP products (Lievens et al. 2015; Miernecki et al. 2014), which
778 both provide an accuracy of $0.04 \text{ m}^3 \text{ m}^{-3}$ (Zhang et al. 2019). However, the actual observation error of
779 these two products typically depends on the spatial location and time of the year (RMSD varying between

780 0.035 and 0.056 m³ m⁻³ for several retrieval configurations) (Brocca et al. 2012). According to Purdy et
781 al. (2018), the ET simulated by PT-JPL_{SM} using the 9 km SM_L3_P_E data showed an inferior agreement
782 ($R^2= 0.47$) but a relatively low RMSD (0.77 mm d⁻¹), due to the SMAP errors in the grid cell with soil
783 heterogeneity and the climatological differences between model SM forecasts and SMAP SM (Reichle
784 and Koster 2004). We rescaled the ET_{PM} to the probability distribution of the ET_{LPJ} through a cumulative
785 distribution function (CDF) to correct the potential seasonal biases of ET_{PM} before assimilation.

786 Second, there is large uncertainty in the influence of root zone SM as the source of water available
787 to plants (Albergel et al. 2008; Bonan et al. 2020). Our GPP results of cropland sites were largely
788 influenced by US-Ne1, an irrigate site. This site maintained high annual GPP in 2012 despite the drought
789 (Figure S4). However, the SMOS SM in 2012 had a lower surface SM annual mean than the site
790 observations likely because the detected soil layer (0-50 cm) of the site observation is deeper than that of
791 the satellite retrieval and the cumulative deep soil moisture due to the regular irrigation was higher than
792 the surface SM that could easily be vaporized during the drought period (Figure S4). Therefore, the
793 influence of deep SM of some cropland sites during the drought years induced large simulation errors and
794 unsatisfactory assimilation performance. Moreover, some deep-rooted forests maintain a high LAI during
795 drought by absorbing deep SM (>2 m) and groundwater (Zhang et al. 2016). Thus, joint assimilation of
796 the LAI and SM may eliminate a portion of the underestimation of GPP of such vegetation in drought
797 periods. Therefore, further research is needed on how to optimally utilize satellite SM data for improving
798 GPP and ET simulations.

799 Third, the problem of mixed pixels and mismatches in the observation footprints may also have an
800 influence on the accuracy of estimated GPP and ET. The 5 km spatial resolution of the GLASS LAI ,9
801 km of SMAP, and 25 km of SMOS products cannot capture the sub-grid-scale condition, especially in
802 grid cells for complex land surfaces or strong soil heterogeneity. To ensure the consistency of the grid-
803 cell representativeness for the LAI and SM, the interpolation result in errors that propagate through the
804 modeling and assimilation, causing the accumulation of output errors (Nijssen and Lettenmaier 2004).
805 Moreover, the shrubland in the LPJ-DGVM was most likely simulated as C4 grassland in the
806 hydrothermal condition of semi-arid and arid regions. In contrast, the shrubland tended to be hybrid
807 vegetation types (grassland mixed with other types of forest vegetation) in the hydrothermal condition of
808 humid and sub-dry humid regions, and the simulated canopy height is closer to the real condition of
809 shrubland. This might also be the reason for the superior performance of ET_{LPJ} and assimilation results
810 of shrubland sites in humid and sub-dry humid regions.

811 When assimilating multiple data streams, all data streams could be in the same optimization
812 (simultaneous assimilation) or use a sequential (step-by-step) approach. Mathematically, simultaneous
813 optimization is optimal because strong parametric connections are maintained between different
814 processes. However, complications may arise due to computational constraints related to the inversion of
815 large matrices or the requirement of numerous simulations, particularly for global datasets (e.g. Peylin et
816 al.,2016), and due to the “weight” of different data streams in the optimization (e.g. Wutzler and
817 Carvalhais, 2014). This is particularly true when considering a regional-to-global-scale, multiple site
818 optimization of a complex model that contains many parameters, and which typically takes on the order

819 of minutes to an hour to run a one-year simulation. In practice, it is very difficult to define a probability
820 distribution that properly characterizes the model structural uncertainty and observation errors accounting
821 for biases and non-Gaussian distributions. Nevertheless, a step-wise assimilation may be useful in dealing
822 with possible inconsistencies on a temporary basis, since parameter error covariance matrix must be
823 propagated at each step. It's worth noting that the deviation between the model and observational data
824 should be solved in the process of step-wise assimilation, such as the joint assimilation in this study, the
825 satellite observations and model simulation were fitting through the CDF method so that the first step
826 assimilation will strongly constrain the uncertainty of parameters related to phenology and carbon flux
827 and propagate to the second step . Alternative solutions were found for water -related parameters through
828 soil moisture, providing a better fit for all data streams.

829 The sequence of assimilation is essential in the step-wise assimilation, and if the first observation
830 contains a strong bias, then the associated error correlation will also propagate through the first
831 assimilation. If the autocorrelation in the observation error, or the correlation between the data stream
832 errors is not considered, it is likely that the posterior simulation has been overturned. That is, we
833 overestimate the reduction in parametric uncertainty. If two observational data are less uncertainty (i.e.,
834 high precision of observation data), and the model of deviation is smaller (depend on the spatial scale and
835 inversion method). Moreover, the correlation of these observations is stronger, and contain enough spatio-
836 temporal information to limit all the parameters optimization accurately, the step-wise assimilation
837 performance is basically the same as that of simultaneous assimilation.

838 **6. Conclusions**

839 We developed an assimilation system LPJ-VSJA that integrates GLASS LAI, SMOS SM, and
840 SMAP SM data to improve GPP and ET estimates globally. The system was designed to assimilate two
841 SM products (SMOS and SMAP) into the integrated model - LPJ-PM for both dry and humid regions
842 through separate and joint assimilation. The results show that the joint constraints provided by vegetation
843 and soil variable strategies improve model simulations. Both the original and joint assimilation results for
844 GPP and ET in semi-arid and arid regions performed better than those in humid and dry-sub humid regions,
845 and the LPJ-PM that emphasized the SM information is more suitable for the water-limited regions. For
846 ET assimilation, the different SM products influence assimilation performance, and SMAP SM possesses
847 a slight advantage in most vegetation types and in both dry and humid regions. Our global LPJ-VSJA
848 GPP and ET products have relatively higher accuracy than other products, especially in water-limited
849 regions with lower ET values.

850 **Data availability**

851 The LPJ-DGVM v4.1 version code (LPJ-ML) and example configurations are public available via the
852 project homepage (<https://github.com/PIK-LPJmL/LPJmL>). We used the 3.01 version of LPJ-DGVM,
853 which removed the agricultural management module. The access of all the input and validation dataset of
854 assimilation system have been described in article. The assimilation method code configured by Fortran
855 platform could be provided by contacting the X.T co-author. The modified code of LPJ-PM model and

856 the underlying and global LPJ-VSJA GPP and ET data can be obtained by contacting the lead author of
857 this manuscript.

858 **Author contributions**

859 S.L. and L.Z. designed the experiment and wrote the paper with support from all coauthors. S.L. and R.M.
860 implemented the codes necessary for the experiments. J.X. contributed to the structure of the article and
861 comparison of assimilation performance between the SMOS and SMAP experiments. X.T provided the
862 POD-En4DVAR method and the code. M.Y contributed to the validation and analysis of the results. All
863 the authors contributed to the synthesis of results and key conclusions.

864 **Competing interests**

865 The authors declare that they have no known competing financial interests or personal relationships that
866 could have appeared to influence the work reported in this paper.

867

868 **Financial support**

869 S.L., L.Z., R.M., and M.Y. were funded by the National Natural Science Foundation of China (Grant No.
870 41771392; PI Li Zhang) and (Grant No. 41901364; PI Min Yan).

871

872 **References**

873 Albergel, C., Rüdiger, C., Pellarin, T., Calvet, J.-C., Fritz, N., Froissard, F., Suquia, D., Petitpa, A., Pignatelli, B., & Martin,
874 E. (2008). From near-surface to root-zone soil moisture using an exponential filter: an assessment of the method based
875 on in-situ observations and model simulations. *Hydrology and Earth System Sciences*, *12*, 1323-1337

876 [Albergel, C., Calvet, J.-C., Mahfouf, J.-F., Rüdiger, C., Barbu, A. L., Lafont, S., Roujean, J.-L., Walker, J. P., Crapeau,](#)
877 [M., and Wigneron, J.-P.: Monitoring of water and carbon fluxes using a land data assimilation system: a case study for](#)
878 [southwestern France, Hydrol. Earth Syst. Sci., 14, 1109–1124, https://doi.org/10.5194/hess-14-1109-2010, 2010.](#)

879 [Albergel, C., Zheng, Y., Bonan, B., Dutra, E., Rodríguez-Fernández, N., Munier, S., Draper, C., de Rosnay, P., Muñoz-](#)
880 [Sabater, J., Balsamo, G., Fairbairn, D., Meurey, C., and Calvet, J.-C.: Data assimilation for continuous global assessment](#)
881 [of severe conditions over terrestrial surfaces, Hydrol. Earth Syst. Sci., 24, 4291–4316, https://doi.org/10.5194/hess-24-](#)
882 [4291-2020, 2020.](#)

883 Anav, A., Friedlingstein, P., Beer, C., Ciais, P., Harper, A., Jones, C., Murray - Tortarolo, G., Papale, D., Parazoo, N.C.,
884 & Peylin, P. (2015). Spatiotemporal patterns of terrestrial gross primary production: A review. *Reviews of Geophysics*,
885 *53*, 785-818

886 [Barth, A., Beckers, J.-M., Troupin, C., Alvera-Azcárate, A., & Vandenbulcke, L. \(2014\). divand-1.0: n-dimensional](#)
887 [variational data analysis for ocean observations. Geoscientific Model Development, 7, 225-241](#)

888 Blyverket, J., Hamer, P.D., Bertino, L., Albergel, C., Fairbairn, D., & Lahoz, W.A. (2019). An Evaluation of the EnKF
889 vs. EnOI and the Assimilation of SMAP, SMOS and ESA CCI Soil Moisture Data over the Contiguous US. *Remote*
890 *Sensing*, *11*, 478

891 Bonan, B., Albergel, C., Zheng, Y., Barbu, A.L., Fairbairn, D., Munier, S., & Calvet, J.-C. (2020). An ensemble square
892 root filter for the joint assimilation of surface soil moisture and leaf area index within the Land Data Assimilation System
893 LDAS-Monde: application over the Euro-Mediterranean region. *Hydrology and Earth System Sciences*, *24*, 325-347

894 Bonan, G., Williams, M., Fisher, R., & Oleson, K. (2014). Modeling stomatal conductance in the earth system: linking
895 leaf water-use efficiency and water transport along the soil–plant–atmosphere continuum. *Geoscientific Model*
896 *Development*, *7*, 2193-2222

897 Brocca, L., Tullo, T., Melone, F., Moramarco, T., & Morbidelli, R. (2012). Catchment scale soil moisture spatial–
898 temporal variability. *Journal of hydrology*, *422*, 63-75

899 Burgin, M.S., Colliander, A., Njoku, E.G., Chan, S.K., Cabot, F., Kerr, Y.H., Bindlish, R., Jackson, T.J., Entekhabi, D.,
900 & Yueh, S.H. (2017). A comparative study of the SMAP passive soil moisture product with existing satellite-based soil
901 moisture products. *IEEE Transactions on Geoscience and Remote Sensing*, *55*, 2959-2971

902 Caires, S., & Sterl, A. (2003). Validation of ocean wind and wave data using triple collocation. *Journal of geophysical*
903 *research: oceans*, *108*

904 Chan, S.K., Bindlish, R., O'Neill, P.E., Njoku, E., Jackson, T., Colliander, A., Chen, F., Burgin, M., Dunbar, S., &
905 Piepmeier, J. (2016). Assessment of the SMAP passive soil moisture product. *IEEE Transactions on Geoscience and*
906 *Remote Sensing*, *54*, 4994-5007

907 Cui, C., Xu, J., Zeng, J., Chen, K.-S., Bai, X., Lu, H., Chen, Q., & Zhao, T. (2018). Soil moisture mapping from satellites:
908 An intercomparison of SMAP, SMOS, FY3B, AMSR2, and ESA CCI over two dense network regions at different spatial
909 scales. *Remote Sensing*, *10*, 33

- 910 Desai, A.R., Moore, D.J., Ahue, W.K., Wilkes, P.T., De Wekker, S.F., Brooks, B.G., Campos, T.L., Stephens, B.B.,
911 Monson, R.K., & Burns, S.P. (2011). Seasonal pattern of regional carbon balance in the central Rocky Mountains from
912 surface and airborne measurements. *Journal of Geophysical Research: Biogeosciences*, 116
- 913 Draper, C., Mahfouf, J.-F., Calvet, J.-C., Martin, E., & Wagner, W. (2011). Assimilation of ASCAT near-surface soil
914 moisture into the SIM hydrological model over France. *Hydrology and Earth System Sciences*, 15, 3829-3841
- 915 Entekhabi, D., Njoku, E.G., O'Neill, P.E., Kellogg, K.H., Crow, W.T., Edelstein, W.N., Entin, J.K., Goodman, S.D.,
916 Jackson, T.J., & Johnson, J. (2010). The soil moisture active passive (SMAP) mission. *Proceedings of the IEEE*, 98,
917 704-716
- 918 Etheridge, D.M., Steele, L., Langenfelds, R.L., Francey, R.J., Barnola, J.M., & Morgan, V. (1996). Natural and
919 anthropogenic changes in atmospheric CO₂ over the last 1000 years from air in Antarctic ice and firn. *Journal of*
920 *Geophysical Research: Atmospheres*, 101, 4115-4128
- 921 Evensen, G. (2004). Sampling strategies and square root analysis schemes for the EnKF. *Ocean dynamics*, 54, 539-560
- 922 [Exbrayat, J.F., Bloom, A.A., Carvalhais, N. et al. Understanding the Land Carbon Cycle with Space Data: Current Status](https://doi.org/10.1007/s10712-019-09506-2)
923 [and Prospects. Surv Geophys 40, 735–755 \(2019\). https://doi.org/10.1007/s10712-019-09506-2](https://doi.org/10.1007/s10712-019-09506-2)
- 924 Fang, H., Baret, F., Plummer, S., & Schaepman - Strub, G. (2019). An overview of global leaf area index (LAI): Methods,
925 products, validation, and applications. *Reviews of Geophysics*, 57, 739-799
- 926 Fang, H., Beaudoin, H.K., Rodell, M., Teng, W.L., & Vollmer, B.E. (2009). Global Land data assimilation system
927 (GLDAS) products, services and application from NASA hydrology data and information services center (HDISC). In,
928 *ASPRS 2009 Annual Conference, Baltimore, Maryland* (pp. 8-13)
- 929 Fang, H., & Liang, S. (2005). A hybrid inversion method for mapping leaf area index from MODIS data: Experiments
930 and application to broadleaf and needleleaf canopies. *Remote Sensing of Environment*, 94, 405-424
- 931 Feng, F., Chen, J., Li, X., Yao, Y., Liang, S., Liu, M., Zhang, N., Guo, Y., Yu, J., & Sun, M. (2015). Validity of five
932 satellite-based latent heat flux algorithms for semi-arid ecosystems. *Remote Sensing*, 7, 16733-16755
- 933 Friedl, M.A., Sulla-Menashe, D., Tan, B., Schneider, A., Ramankutty, N., Sibley, A., & Huang, X. (2010). MODIS
934 Collection 5 global land cover: Algorithm refinements and characterization of new datasets. *Remote Sensing of*
935 *Environment*, 114, 168-182
- 936 Gokmen, M., Vekerdy, Z., Verhoef, A., Verhoef, W., Batelaan, O., & Van der Tol, C. (2012). Integration of soil moisture
937 in SEBS for improving evapotranspiration estimation under water stress conditions. *Remote Sensing of Environment*,
938 121, 261-274
- 939 Gonsamo, A., & Chen, J.M. (2011). Evaluation of the GLC2000 and NALC2005 land cover products for LAI retrieval
940 over Canada. *Canadian Journal of Remote Sensing*, 37, 302-313
- 941 Haxeltine, A., & Prentice, I.C. (1996). BIOME3: An equilibrium terrestrial biosphere model based on ecophysiological
942 constraints, resource availability, and competition among plant functional types. *Global biogeochemical cycles*, 10, 693-
943 709
- 944 Hayes, D.J., Turner, D.P., Stinson, G., McGuire, A.D., Wei, Y., West, T.O., Heath, L.S., De Jong, B., McConkey, B.G.,
945 & Birdsey, R.A. (2012). Reconciling estimates of the contemporary North American carbon balance among terrestrial
946 biosphere models, atmospheric inversions, and a new approach for estimating net ecosystem exchange from inventory -
947 based data. *Global Change Biology*, 18, 1282-1299

- 948 He, L., Chen, J.M., Liu, J., Bélair, S., & Luo, X. (2017). Assessment of SMAP soil moisture for global simulation of
949 gross primary production. *Journal of Geophysical Research: Biogeosciences*, *122*, 1549-1563
- 950 Huang, C., Li, Y., Gu, J., Lu, L., & Li, X. (2015). Improving estimation of evapotranspiration under water-limited
951 conditions based on SEBS and MODIS data in arid regions. *Remote Sensing*, *7*, 16795-16814
- 952 Ines, A.V., Das, N.N., Hansen, J.W., & Njoku, E.G. (2013). Assimilation of remotely sensed soil moisture and vegetation
953 with a crop simulation model for maize yield prediction. *Remote Sensing of Environment*, *138*, 149-164
- 954 Jacqueline, E., Al Bitar, A., Mialon, A., Kerr, Y., Quesney, A., Cabot, F., & Richaume, P. (2010). SMOS CATDS level
955 3 global products over land. In *Remote Sensing for Agriculture, Ecosystems, and Hydrology XII* (p. 78240K):
956 International Society for Optics and Photonics
- 957 Kaminski, T., Scholze, M., Vossbeck, M., Knorr, W., Buchwitz, M., & Reuter, M. (2017). Constraining a terrestrial
958 biosphere model with remotely sensed atmospheric carbon dioxide. *Remote Sensing of Environment*, *203*, 109-124
- 959 Kato, T., Knorr, W., Scholze, M., Veenendaal, E., Kaminski, T., Kattge, J., & Gobron, N. (2013). Simultaneous
960 assimilation of satellite and eddy covariance data for improving terrestrial water and carbon simulations at a semi-arid
961 woodland site in Botswana. *Biogeosciences*, *10*, 789-802
- 962 Keeling, C.D., Whorf, T.P., Wahlen, M., & Van der Plichtt, J. (1995). Interannual extremes in the rate of rise of
963 atmospheric carbon dioxide since 1980. *Nature*, *375*, 666-670
- 964 Keller, M., Schimel, D.S., Hargrove, W.W., & Hoffman, F.M. (2008). A continental strategy for the National Ecological
965 Observatory Network. *Frontiers in Ecology and the Environment*, *6*, 282-284
- 966 Kganyago, M., Mhangara, P., Alexandridis, T., Laneve, G., Ovakoglou, G., & Mashiyi, N. (2020). Validation of sentinel-
967 2 leaf area index (LAI) product derived from SNAP toolbox and its comparison with global LAI products in an African
968 semi-arid agricultural landscape. *Remote Sensing Letters*, *11*, 883-892
- 969 Khan, M.S., Liaqat, U.W., Baik, J., & Choi, M. (2018). Stand-alone uncertainty characterization of GLEAM, GLDAS
970 and MOD16 evapotranspiration products using an extended triple collocation approach. *Agricultural and Forest
971 Meteorology*, *252*, 256-268
- 972 Kim, H., Parinussa, R., Konings, A.G., Wagner, W., Cosh, M.H., Lakshmi, V., Zohaib, M., & Choi, M. (2018). Global-
973 scale assessment and combination of SMAP with ASCAT (active) and AMSR2 (passive) soil moisture products. *Remote
974 Sensing of Environment*, *204*, 260-275
- 975 Koster, R.D., Crow, W.T., Reichle, R.H., & Mahanama, S.P. (2018). Estimating basin - scale water budgets with SMAP
976 soil moisture data. *Water resources research*, *54*, 4228-4244
- 977 Law, B., Falge, E., Gu, L.v., Baldocchi, D., Bakwin, P., Berbigier, P., Davis, K., Dolman, A., Falk, M., & Fuentes, J.
978 (2002). Environmental controls over carbon dioxide and water vapor exchange of terrestrial vegetation. *Agricultural and
979 Forest Meteorology*, *113*, 97-120
- 980 Lee, H., Seo, D.-J., & Koren, V. (2011). Assimilation of streamflow and in situ soil moisture data into operational
981 distributed hydrologic models: Effects of uncertainties in the data and initial model soil moisture states. *Advances in
982 water resources*, *34*, 1597-1615
- 983 Li, B., & Rodell, M. (2013). Spatial variability and its scale dependency of observed and modeled soil moisture over
984 different climate regions. *Hydrology and Earth System Sciences*, *17*, 1177-1188

- 985 Li C, Tang G, Hong Y. Cross-evaluation of ground-based, multi-satellite and reanalysis precipitation products:
986 Applicability of the Triple Collocation method across Mainland China[J]. *Journal of Hydrology*, 2018, 562: 71-83.
- 987 Li, S., Wang, G., Sun, S., Chen, H., Bai, P., Zhou, S., Huang, Y., Wang, J., & Deng, P. (2018). Assessment of multi-
988 source evapotranspiration products over china using eddy covariance observations. *Remote Sensing*, 10, 1692
- 989 Li, S., Zhang, L., Ma, R., Yan, M., & Tian, X. (2020). Improved ET assimilation through incorporating SMAP soil
990 moisture observations using a coupled process model: A study of US arid and semiarid regions. *Journal of hydrology*,
991 590, 125402
- 992 Li, X., Cheng, G., Liu, S., Xiao, Q., Ma, M., Jin, R., Che, T., Liu, Q., Wang, W., & Qi, Y. (2013). Heihe watershed allied
993 telemetry experimental research (HiWATER): Scientific objectives and experimental design. *Bulletin of the American*
994 *Meteorological Society*, 94, 1145-1160
- 995 Li, X., Mao, F., Du, H., Zhou, G., Xu, X., Han, N., Sun, S., Gao, G., & Chen, L. (2017). Assimilating leaf area index of
996 three typical types of subtropical forest in China from MODIS time series data based on the integrated ensemble Kalman
997 filter and PROSAIL model. *ISPRS Journal of Photogrammetry and Remote Sensing*, 126, 68-78
- 998 Li, X., & Xiao, J. (2019). A global, 0.05-degree product of solar-induced chlorophyll fluorescence derived from OCO-
999 2, MODIS, and reanalysis data. *Remote Sensing*, 11, 517
- 1000 Liang, S., Zhao, X., Liu, S., Yuan, W., Cheng, X., Xiao, Z., Zhang, X., Liu, Q., Cheng, J., & Tang, H. (2013). A long-
1001 term Global LAnd Surface Satellite (GLASS) data-set for environmental studies. *International Journal of Digital Earth*,
1002 6, 5-33
- 1003 Lievens, H., Tomer, S.K., Al Bitar, A., De Lannoy, G.J., Drusch, M., Dumedah, G., Franssen, H.-J.H., Kerr, Y.H.,
1004 Martens, B., & Pan, M. (2015). SMOS soil moisture assimilation for improved hydrologic simulation in the Murray
1005 Darling Basin, Australia. *Remote Sensing of Environment*, 168, 146-162
- 1006 Ling, X.-L., Fu, C.-B., Yang, Z.-L., & Guo, W.-D. (2019). Comparison of different sequential assimilation algorithms
1007 for satellite-derived leaf area index using the Data Assimilation Research Testbed (version Lanai). *Geoscientific Model*
1008 *Development*, 12, 3119-3133
- 1009 Liu, L., Gudmundsson, L., Hauser, M., Qin, D., Li, S., & Seneviratne, S.I. (2020). Soil moisture dominates dryness stress
1010 on ecosystem production globally. *Nature communications*, 11, 1-9
- 1011 Liu, Y., Xiao, J., Ju, W., Zhu, G., Wu, X., Fan, W., Li, D., & Zhou, Y. (2018). Satellite-derived LAI products exhibit
1012 large discrepancies and can lead to substantial uncertainty in simulated carbon and water fluxes. *Remote Sensing of*
1013 *Environment*, 206, 174-188
- 1014 Ma, H., Huang, J., Zhu, D., Liu, J., Su, W., Zhang, C., & Fan, J. (2013). Estimating regional winter wheat yield by
1015 assimilation of time series of HJ-1 CCD NDVI into WOFOST-ACRM model with Ensemble Kalman Filter.
1016 *Mathematical and Computer Modelling*, 58, 759-770
- 1017 Ma, R., Zhang, L., Tian, X., Zhang, J., Yuan, W., Zheng, Y., Zhao, X., & Kato, T. (2017). Assimilation of remotely-
1018 sensed leaf area index into a dynamic vegetation model for gross primary productivity estimation. *Remote Sensing*, 9,
1019 188
- 1020 MacBean, N., Peylin, P., Chevallier, F., Scholze, M., & Schürmann, G. (2016). Consistent assimilation of multiple data
1021 streams in a carbon cycle data assimilation system. *Geoscientific Model Development*, 9, 3569-3588

- 1022 Martens, B., Miralles, D.G., Lievens, H., Schalie, R.v.d., De Jeu, R.A., Fernández-Prieto, D., Beck, H.E., Dorigo, W.A.,
 1023 & Verhoest, N.E. (2017). GLEAM v3: Satellite-based land evaporation and root-zone soil moisture. *Geoscientific Model*
 1024 *Development, 10*, 1903-1925
- 1025 Miernecki, M., Wigneron, J.-P., Lopez-Baeza, E., Kerr, Y., De Jeu, R., De Lannoy, G.J., Jackson, T.J., O'Neill, P.E.,
 1026 Schwank, M., & Moran, R.F. (2014). Comparison of SMOS and SMAP soil moisture retrieval approaches using tower-
 1027 based radiometer data over a vineyard field. *Remote Sensing of Environment, 154*, 89-101
- 1028 Miralles, D.G., Jiménez, C., Jung, M., Michel, D., Ershadi, A., McCabe, M., Hirschi, M., Martens, B., Dolman, A.J., &
 1029 Fisher, J.B. (2016). The WACMOS-ET project—Part 2: Evaluation of global terrestrial evaporation data sets. *Hydrology*
 1030 *and Earth System Sciences, 20*, 823-842
- 1031 Mitchell, H.L., Houtekamer, P.L., & Pellerin, G. (2002). Ensemble size, balance, and model-error representation in an
 1032 ensemble Kalman filter. *Monthly weather review, 130*, 2791-2808
- 1033 Mu, Q., Zhao, M., Heinsch, F.A., Liu, M., Tian, H., & Running, S.W. (2007). Evaluating water stress controls on primary
 1034 production in biogeochemical and remote sensing based models. *Journal of Geophysical Research: Biogeosciences, 112*
- 1035 New, M., Hulme, M., & Jones, P. (2000). Representing twentieth-century space–time climate variability. Part II:
 1036 Development of 1901–96 monthly grids of terrestrial surface climate. *Journal of climate, 13*, 2217-2238
- 1037 Nijssen, B., & Lettenmaier, D.P. (2004). Effect of precipitation sampling error on simulated hydrological fluxes and
 1038 states: Anticipating the Global Precipitation Measurement satellites. *Journal of Geophysical Research: Atmospheres,*
 1039 *109*
- 1040 O'Neill, P., Entekhabi, D., Njoku, E., & Kellogg, K. (2010). The NASA soil moisture active passive (SMAP) mission:
 1041 Overview. In, *2010 IEEE International Geoscience and Remote Sensing Symposium* (pp. 3236-3239): IEEE
- 1042 O'Carroll, A.G., Eyre, J.R., & Saunders, R.W. (2008). Three-way error analysis between AATSR, AMSR-E, and in situ
 1043 sea surface temperature observations. *Journal of atmospheric and oceanic technology, 25*, 1197-1207
- 1044 [Pan, H.; Chen, Z.; de Wit, A.; Ren, J. Joint Assimilation of Leaf Area Index and Soil Moisture from Sentinel-1 and](#)
 1045 [Sentinel-2 Data into the WOFOST Model for Winter Wheat Yield Estimation. Sensors 2019, 19, 3161.](#)
- 1046 Pardo, N., Sánchez, M.L., Timmermans, J., Su, Z., Pérez, I.A., & García, M.A. (2014). SEBS validation in a Spanish
 1047 rotating crop. *Agricultural and Forest Meteorology, 195*, 132-142
- 1048 Petropoulos, G.P., Ireland, G., & Barrett, B. (2015). Surface soil moisture retrievals from remote sensing: Current status,
 1049 products & future trends. *Physics and Chemistry of the Earth, Parts A/B/C, 83*, 36-56
- 1050 Pipunic, R., Walker, J., & Western, A. (2008). Assimilation of remotely sensed data for improved latent and sensible
 1051 heat flux prediction: A comparative synthetic study. *Remote Sensing of Environment, 112*, 1295-1305
- 1052 Purdy, A.J., Fisher, J.B., Goulden, M.L., Colliander, A., Halverson, G., Tu, K., & Famiglietti, J.S. (2018). SMAP soil
 1053 moisture improves global evapotranspiration. *Remote Sensing of Environment, 219*, 1-14
- 1054 [Rahman, A.; Maggioni, V.; Zhang, X.; Houser, P.; Sauer, T.; Mocko, D.M. The Joint Assimilation of Remotely Sensed](#)
 1055 [Leaf Area Index and Surface Soil Moisture into a Land Surface Model. Remote Sens. 2022, 14, 437.](#)
 1056 <https://doi.org/10.3390/rs14030437>
- 1057 Rüdiger, C., Albergel, C., Mahfouf, J.F., Calvet, J.C., & Walker, J.P. (2010). Evaluation of the observation operator
 1058 Jacobian for leaf area index data assimilation with an extended Kalman filter. *Journal of Geophysical Research:*
 1059 *Atmospheres, 115*

- 1060 Reichle, R.H., De Lannoy, G.J., Liu, Q., Koster, R.D., Kimball, J.S., Crow, W.T., Ardizzone, J.V., Chakraborty, P.,
1061 Collins, D.W., & Conaty, A.L. (2017). Global assessment of the SMAP level-4 surface and root-zone soil moisture
1062 product using assimilation diagnostics. *Journal of Hydrometeorology*, 18, 3217-3237
- 1063 Reichle, R.H., & Koster, R.D. (2004). Bias reduction in short records of satellite soil moisture. *Geophysical Research*
1064 *Letters*, 31
- 1065 Rienecker, M.M., Suarez, M.J., Gelaro, R., Todling, R., Bacmeister, J., Liu, E., Bosilovich, M.G., Schubert, S.D., Takacs,
1066 L., & Kim, G.-K. (2011). MERRA: NASA's modern-era retrospective analysis for research and applications. *Journal of*
1067 *climate*, 24, 3624-3648
- 1068 Running, S.W., Nemani, R.R., Heinsch, F.A., Zhao, M., Reeves, M., & Hashimoto, H. (2004). A continuous satellite-
1069 derived measure of global terrestrial primary production. *Bioscience*, 54, 547-560
- 1070 Scholze, M., Buchwitz, M., Dorigo, W., Guanter, L., and Quegan, S.: Reviews and syntheses: Systematic Earth
1071 observations for use in terrestrial carbon cycle data assimilation systems, Biogeosciences, 14, 3401–3429,
1072 <https://doi.org/10.5194/bg-14-3401-2017>, 2017.
- 1073 Seneviratne, S.I., Corti, T., Davin, E.L., Hirschi, M., Jaeger, E.B., Lehner, I., Orlowsky, B., & Teuling, A.J. (2010).
1074 Investigating soil moisture–climate interactions in a changing climate: A review. *Earth-Science Reviews*, 99, 125-161
- 1075 Sitch, S., Smith, B., Prentice, I.C., Arneth, A., Bondeau, A., Cramer, W., Kaplan, J.O., Levis, S., Lucht, W., & Sykes,
1076 M.T. (2003). Evaluation of ecosystem dynamics, plant geography and terrestrial carbon cycling in the LPJ dynamic
1077 global vegetation model. *Global Change Biology*, 9, 161-185
- 1078 Stoffelen, A. (1998). Toward the true near - surface wind speed: Error modeling and calibration using triple collocation.
1079 *Journal of geophysical research: oceans*, 103, 7755-7766
- 1080 Sun, P., Wu, Y., Xiao, J., Hui, J., Hu, J., Zhao, F., Qiu, L., & Liu, S. (2019). Remote sensing and modeling fusion for
1081 investigating the ecosystem water-carbon coupling processes. *Science of the total environment*, 697, 134064
- 1082 Taylor, K.E. (2001). Summarizing multiple aspects of model performance in a single diagram. *Journal of Geophysical*
1083 *Research: Atmospheres*, 106, 7183-7192
- 1084 Tian, S., Renzullo, L.J., Van Dijk, A.I., Tregoning, P., & Walker, J.P. (2019). Global joint assimilation of GRACE and
1085 SMOS for improved estimation of root-zone soil moisture and vegetation response. *Hydrology and Earth System*
1086 *Sciences*, 23, 1067-1081
- 1087 Tian, X., & Feng, X. (2015). A non-linear least squares enhanced POD-4DVar algorithm for data assimilation. *Tellus A:*
1088 *Dynamic Meteorology and Oceanography*, 67, 25340
- 1089 Tian, X., Xie, Z., Dai, A., Jia, B., & Shi, C. (2010). A microwave land data assimilation system: Scheme and preliminary
1090 evaluation over China. *Journal of Geophysical Research: Atmospheres*, 115
- 1091 Tian, X., Xie, Z., Dai, A., Shi, C., Jia, B., Chen, F., & Yang, K. (2009). A dual - pass variational data assimilation
1092 framework for estimating soil moisture profiles from AMSR - E microwave brightness temperature. *Journal of*
1093 *Geophysical Research: Atmospheres*, 114
- 1094 Tian, X., Xie, Z., Liu, Y., Cai, Z., Fu, Y., Zhang, H., & Feng, L. (2014). A joint data assimilation system (Tan-Tracker)
1095 to simultaneously estimate surface CO₂ fluxes and 3-D atmospheric CO₂ concentrations from observations.
1096 *Atmospheric Chemistry and Physics*, 14, 13281-13293

- 1097 Tian, X., Xie, Z., & Sun, Q. (2011). A POD-based ensemble four-dimensional variational assimilation method. *Tellus*
1098 *A: Dynamic Meteorology and Oceanography*, 63, 805-816
- 1099 Trugman, A., Medvigy, D., Mankin, J., & Anderegg, W. (2018). Soil moisture stress as a major driver of carbon cycle
1100 uncertainty. *Geophysical Research Letters*, 45, 6495-6503
- 1101 Turner, D.P., Ritts, W.D., Cohen, W.B., Gower, S.T., Running, S.W., Zhao, M., Costa, M.H., Kirschbaum, A.A., Ham,
1102 J.M., & Saleska, S.R. (2006). Evaluation of MODIS NPP and GPP products across multiple biomes. *Remote Sensing of*
1103 *Environment*, 102, 282-292
- 1104 Turner, D.P., Ritts, W.D., Cohen, W.B., Maeirsperger, T.K., Gower, S.T., Kirschbaum, A.A., Running, S.W., Zhao, M.,
1105 Wofsy, S.C., & Dunn, A.L. (2005). Site - level evaluation of satellite - based global terrestrial gross primary production
1106 and net primary production monitoring. *Global Change Biology*, 11, 666-684
- 1107 Twine, T.E., Kustas, W., Norman, J., Cook, D., Houser, P., Meyers, T., Prueger, J., Starks, P., & Wesely, M. (2000).
1108 Correcting eddy-covariance flux underestimates over a grassland. *Agricultural and Forest Meteorology*, 103, 279-300
- 1109 Wang, L., Zhu, H., Lin, A., Zou, L., Qin, W., & Du, Q. (2017). Evaluation of the latest MODIS GPP products across
1110 multiple biomes using global eddy covariance flux data. *Remote Sensing*, 9, 418
- 1111 Waring, R.H., & Running, S.W. (2010). *Forest ecosystems: analysis at multiple scales*. Elsevier
- 1112 Wieder, W., Boehnert, J., Bonan, G., & Langseth, M. (2014). RegridDED harmonized world soil database v1. 2. *ORNL*
1113 *DAAC*
- 1114 [Wu, M.; Scholze, M.; Voßbeck, M.; Kaminski, T.; Hoffmann, G. Simultaneous Assimilation of Remotely Sensed Soil
1115 Moisture and FAPAR for Improving Terrestrial Carbon Fluxes at Multiple Sites Using CCDAS. *Remote Sens.* 2019, 11,
1116 27. <https://doi.org/10.3390/rs11010027>](https://doi.org/10.3390/rs11010027)
- 1117 Xiao, J., Chevallier, F., Gomez, C., Guanter, L., Hicke, J.A., Huete, A.R., Ichii, K., Ni, W., Pang, Y., & Rahman, A.F.
1118 (2019). Remote sensing of the terrestrial carbon cycle: A review of advances over 50 years. *Remote Sensing of*
1119 *Environment*, 233, 111383
- 1120 Xiao, Z., Liang, S., & Jiang, B. (2017). Evaluation of four long time-series global leaf area index products. *Agricultural*
1121 *and Forest Meteorology*, 246, 218-230
- 1122 Xiao, Z., Liang, S., Wang, J., Chen, P., Yin, X., Zhang, L., & Song, J. (2013). Use of general regression neural networks
1123 for generating the GLASS leaf area index product from time-series MODIS surface reflectance. *IEEE Transactions on*
1124 *Geoscience and Remote Sensing*, 52, 209-223
- 1125 Xiao, Z., Liang, S., Wang, J., Xiang, Y., Zhao, X., & Song, J. (2016). Long-time-series global land surface satellite leaf
1126 area index product derived from MODIS and AVHRR surface reflectance. *IEEE Transactions on Geoscience and*
1127 *Remote Sensing*, 54, 5301-5318
- 1128 [Xie, Y.; Wang, P.; Sun, H.; Zhang, S.; Li, L. Assimilation of Leaf Area Index and Surface Soil Moisture With the
1129 CERES-Wheat Model for Winter Wheat Yield Estimation Using a Particle Filter Algorithm. *IEEE J. Sel. Top. Appl.*
1130 *Earth Obs. Remote Sens.* 2017, 10, 1303–1316.](https://doi.org/10.1109/JSTARS.2017.2708888)
- 1131 Yan, M., Tian, X., Li, Z., Chen, E., Wang, X., Han, Z., & Sun, H. (2016). Simulation of forest carbon fluxes using model
1132 incorporation and data assimilation. *Remote Sensing*, 8, 567
- 1133 Yang, W., Wang, Y., Liu, X., Zhao, H., Shao, R., & Wang, G. (2020). Evaluation of the rescaled complementary
1134 principle in the estimation of evaporation on the Tibetan Plateau. *Science of the total environment*, 699, 134367

- 1135 Yang, X., Yong, B., Ren, L., Zhang, Y., & Long, D. (2017). Multi-scale validation of GLEAM evapotranspiration
1136 products over China via ChinaFLUX ET measurements. *International Journal of Remote Sensing*, 38, 5688-5709
- 1137 Yilmaz, M.T., & Crow, W.T. (2014). Evaluation of assumptions in soil moisture triple collocation analysis. *Journal of*
1138 *Hydrometeorology*, 15, 1293-1302
- 1139 Yuan, W., Liu, S., Yu, G., Bonnefond, J.-M., Chen, J., Davis, K., Desai, A.R., Goldstein, A.H., Gianelle, D., & Rossi,
1140 F. (2010). Global estimates of evapotranspiration and gross primary production based on MODIS and global
1141 meteorology data. *Remote Sensing of Environment*, 114, 1416-1431
- 1142 Zhang, D.-H., Li, X.-R., Zhang, F., Zhang, Z.-S., & Chen, Y.-L. (2016). Effects of rainfall intensity and intermittency
1143 on woody vegetation cover and deep soil moisture in dryland ecosystems. *Journal of hydrology*, 543, 270-282
- 1144 Zhang, F., & Weng, Y. (2015). Predicting hurricane intensity and associated hazards: A five-year real-time forecast
1145 experiment with assimilation of airborne Doppler radar observations. *Bulletin of the American Meteorological Society*,
1146 96, 25-33
- 1147 Zhang, L., Xiao, J., Zheng, Y., Li, S., & Zhou, Y. (2020). Increased carbon uptake and water use efficiency in global
1148 semi-arid ecosystems. *Environmental Research Letters*, 15, 034022
- 1149 [Zhang, X., Huang, X.-Y., Liu, J., Poterjoy, J., Weng, Y., Zhang, F., & Wang, H. \(2014\). Development of an efficient](#)
1150 [regional four-dimensional variational data assimilation system for WRF. *Journal of atmospheric and oceanic technology*,](#)
1151 [31, 2777-2794](#)
- 1152 Zhang, R., Kim, S., & Sharma, A. (2019). A comprehensive validation of the SMAP Enhanced Level-3 Soil Moisture
1153 product using ground measurements over varied climates and landscapes. *Remote Sensing of Environment*, 223, 82-94
- 1154 Zhao, L., Xia, J., Xu, C.-y., Wang, Z., Sobkowiak, L., & Long, C. (2013). Evapotranspiration estimation methods in
1155 hydrological models. *Journal of Geographical Sciences*, 23, 359-369
- 1156 Zobitz, J., Moore, D.J., Quaife, T., Braswell, B.H., Bergeson, A., Anthony, J.A., & Monson, R.K. (2014). Joint data
1157 assimilation of satellite reflectance and net ecosystem exchange data constrains ecosystem carbon fluxes at a high-
1158 elevation subalpine forest. *Agricultural and Forest Meteorology*, 195, 73-88
- 1159 Zou, L., Zhan, C., Xia, J., Wang, T., & Gippel, C.J. (2017). Implementation of evapotranspiration data assimilation with
1160 catchment scale distributed hydrological model via an ensemble Kalman filter. *Journal of hydrology*, 549, 685-702
- 1161